Systematic Metaproteomics Mapping Reveals Functional and Ecological Landscapes of Human Gut Microbiota Responses to Therapeutic Drugs

Leyuan Li[1,2,8,*], Caitlin M.A. Simopoulos[2], Janice Mayne[2], Zhibin Ning[2], Xin Zhang[1], Mona Hamada[2], James Butcher[2], Joeselle M. Serrana[2,3], Luman Wang[4], Kai Cheng[2], Hongye Qin[2], Krystal Walker[2], Xu Zhang[2], Alain Stintzi[2], Daniel Figeys[2,5,6,7,8,*]

1 State Key Laboratory of Medical Proteomics, Beijing Proteome Research Center, National Center for Protein Sciences (Beijing), Beijing Institute of Lifeomics, 102206 Beijing, China.
2 School of Pharmaceutical Sciences, Ottawa Institute of Systems Biology and Department of Biochemistry, Microbiology and Immunology, Faculty of Medicine, University of Ottawa, Ottawa, ON K1H 8M5, Canada.
3 Department of Environmental Science (ACES), and the Stockholm University Center for Circular and Sustainable Systems (SUCCeSS), Stockholm University, 106 91 Stockholm, Sweden.
4 Department of Health Informatics and Management, School of Health Humanities, Peking University, Beijing 100191, China
5 Quadram Institute Bioscience, Norwich Research Park, Norwich, Norfolk, UK.
6 University of East Anglia, Norwich, Norfolk, UK.
7 Lead contact (Requests for further information and resources should be directed to and will be fulfilled by the lead contact, Daniel Figeys (dfigeys@uottawa.ca).
8 These authors contributed equally.
* Correspondence: L.L: lileyuan@ncpsb.org.cn, D.F.: dfigeys@uottawa.ca

SUMMARY

Therapeutic compounds significantly alter the composition of the gut microbiota, yet their functional and ecological impacts, particularly at the protein level, remain largely unexplored. In this study, we systematically mapped metaproteomic responses of *ex vivo* human gut microbiota to 312 compounds, generating 4.6 million microbial protein responses, available as an interactive resource (https://shiny.imetalab.ca/MPR_Viz/). Across protein-level, taxonomic composition-level, and ecosystem-level analyses, we simultaneously identified metaproteomic shifts in 47 compounds, a tri-stability taxonomic landscape, and, using our PhyloFunc beta-diversity metric, three distinct functional community state types with cross-individual ecological consistency. Notably, neuropharmaceuticals triggered profound metaproteomic alterations, marked by a decline in functional redundancy (FR) and an increase in antimicrobial resistance proteins (ARPs), shifting the community to alternative functional state on the functional landscape. We validated that enhancing FR maintained a microbiota's resilience against neuropharmaceutical-

induced ARP increase. These findings establish a novel landscape-based framework for understanding microbiome resilience and advancing targeted therapeutic interventions.

INTRODUCTION

The development of human-targeted drugs typically focuses on mechanisms of drug interactions with human protein targets. However, it is often overlooked that therapeutic compounds can have profound impacts on our gut microbiotas, known as off-target effects[1]. Studies have revealed the effects of commonly prescribed drugs on single gut bacterial strains[2], microbiome composition[3], function[3,4] and drug metabolism[5,6]. A more recent study has exemplified these findings by demonstrating that non-antibiotic drugs inhibited *Escherichia coli in vitro* and that the microbial functional pathways they targeted were from those targeted by traditional antibiotics[7]. However, it's important to note that although *E. coli* serves as a frequently investigated model organism, our gut ecosystem is primarily populated by obligate anaerobes belonging to the Bacillota and Bacteroidota phyla, drug effects on which remain largely unexplored. Additionally, ecological interactions between gut microbial species can lead to more complicated drug responses compared to responses of single species. A microbial community can obtain resistance against drug perturbation through exposure protection[8] and metabolic cooperation[9], or conversely, drug-disrupted cross-feeding networks may sensitize the drug response of some microbial species that are otherwise unresponsive to the drug[10,11]. A very recent study has comprehensively evaluated such community behaviors through analysis species abundance dynamics under 30 drug treatments using a 32-species synthetic community[12]. Indeed, drugs response involves the complexity of the ecosystem functioning that goes beyond single species survival[13] or overall compositional responses. In other words, a comprehensive analysis of microbiome drug responses which is observed from a functional omics scope will offer a provide deeper insights of the microbial systems ecology.

The drug modes of action that affect functional microbiome ecosystems vary, but they often involve interactions with key microbial proteins or enzymes. During pharmaceutical drug development, many drugs are developed solely based on their effects through interactions with specific human proteins, without considering the fact that species within the human microbiota may contain structurally similar proteins and may thus also be influenced by these drugs. For example, the serotonin transporter (SERT, encoded by *SLC6A4* in humans), responsible for

serotonin uptake in humans, is commonly targeted for pharmaceutical inhibition by neurological drugs such as antidepressants. Interestingly, SERT belongs to the neurotransmitter:sodium symporters (NSS) family, which is conserved from bacteria to humans[14]. Its bacterial homolog, Leucine transporter (LeuT), has been shown to contain a NSS binding site[14], and has actually been used as a model to predict the antidepressant drug-binding specificity to SERT[15]. Such phenomena suggest that comprehensive observation of drug effects on the metaproteome level – the frontline of microbiota-drug interaction – could offer invaluable insights for in-depth exploration of phenotypic microbiome responses on the functional and ecological levels.

Moreover, since therapeutic drugs span a broad array of chemical structures, they are expected to induce a diverse spectrum of microbial ecosystem responses of the gut microbiota. From the scope of systems ecology, a key question arises: are these responses widely distributed across the functional landscape of the microbiome (a map that connects all possible combinations of microbial functional status)? Or do they cluster around distinct stable functional states, as researchers have suggested regarding community structure[16,17]? Understanding such microbiome functional landscape and mapping drug responses onto it holds significant promise for identifying personalized drug treatments. In microbial systems ecology, functional redundancy (FR) refers to the presence of multiple species that can perform similar functions[18]. It is widely believed that FR is positively related to community resilience[19]. This raises the question of whether FR allows the microbiome to maintain resilience by occupying stable functional states within the functional landscape.

To comprehensively map human gut microbiome's drug response landscape, robust experimental approaches are fundamentally required to capture a broad range of microbiome functional states within the landscape under diverse drug treatments. *In vitro* microbiome culturing has emerged as a potent tool for uncovering microbial responses to drugs and identify means to manipulate these responses from interference from host factors. We've previously developed the RapidAIM platform, which maintains the viability and functional individuality of *ex vivo* human gut microbiota and robustly captures microbiome drug responses using metaproteomics[4] - a technique for the large-scale identification and quantification of proteins within a microbiome, providing insights into the functional state and activities of the microbial community. We have continued to scale up the RapidAIM workflow, including live microbiota biobanking[20], cost-effective metaproteomic TMT-labeling[21], and automation[22]. As a result, we have established the RapidAIM 2.0[22] platform for high-throughput metaproteomic analysis of *in vitro* microbiota cultures, which was applied in this research to reveal the functional landscape of microbiota drug responses.

In this study, we performed high-throughput assays of 312 commonly prescribed therapeutic compounds against different individual gut microbiotas using the RapidAIM 2.0 platform, resulting in nearly 2,000 microbiota cultures and tandem mass tag (TMT)-labelled metaproteomic screenings. Subsequent in-depth label-free metaproteomics analysis of 110 compounds that passed the initial screening further detailed over 4.6 million bacterial protein-drug responses, provided as a resource through an interactive Shiny app. We analyzed the functional and ecological landscapes of gut microbiota responses to therapeutic drugs across three hierarchical levels: protein-level, revealing metaproteomic shifts in 47 of the tested compounds with neuropharmaceuticals significantly enriched; taxonomic composition-level, exhibiting a compositional tri-stability landscape; and systems ecological-level, where our recently developed PhyloFunc beta-diveristy metric[23] identified three distinct functional community state types in response to different compounds, demonstrating remarkable systems-level ecological consistency in drug responses across individuals. Notably, specific human-targeted compounds, particularly neuropharmaceuticals, stimulated the expression of microbial antibiotic resistance proteins (ARP), while reducing community-level FR. Building on the functional energy landscape hypothesis, we were able to reduce the neuropharmaceutical-induced ARM increase by introducing a prebiotic into the culture to counteract the FR decrease. These findings underscore the critical need to map the metaproteomic drug response landscape, as it provides a foundational framework for identifying key leverage points to tailor and optimize personalized drug response modulation.

RESULTS

The human gut metaproteome is altered by a diverse array of drugs

In this study, we cultured human gut microbiotas from healthy subjects and exposed them to a collection of therapeutic compounds in our RapidAIM assay. The functional responses were measured using high-throughput metaproteomics (**Figure 1A**). Briefly, the compounds were selected through a multi-step process: we first included 141 drugs with reported impacts on the microbiome based on our in-house database (**Supplementary Table S1**). Subsequently, we cross-referenced this list with the top 200 most prescribed compounds in the US according to literature[24], resulting in the addition of 119 compounds. To ensure comprehensive coverage of drug classes and properties, we expanded the list further with 52 additional compounds by

addressing three additional questions: 1) according to the ATC classification system, are drug classes being adequately presented or further expansion of drug representatives is needed? 2) does each ATC class contain representative compounds of similar and different chemical structures? 3) which drugs are stereoisomers and can be used to test the stereospecific bioactivity and toxicity? Details of the resulting 312 compounds are listed in **Supplementary Table S1**. Assessing the compounds using structure-based clustering suggests a good coverage of drug diversity (**Figure 1B**).

Experiments were conducted using biobanked live human gut microbiotas from six distinct individuals, with each microbiota treated with different compounds in separate wells of 96-well plates, alongside positive and blank controls (2 mg/mL Kestose and the drug solvent DMSO), resulting in a total of 1,920 microbiota cultures. TMT-11plex™ was used for a first-pass screening of compounds that potentially induced functional responses in the microbiomes. A total of 91,641 peptides (average of 10,025 $\pm$ 1,841 peptides per multiplexed TMT set) and 21,859 proteinGroups (average of 5,496 $\pm$ 519 proteinGroups per multiplexed TMT set) were identified from the 192 multiplexed TMT sets of 1920 samples. Overall Principal Component Analysis (PCA) based on proteinGroups showed both inter-individual differences in metaproteomics and the alteration of metaproteomes by a subset of compounds (**Figure 1C-D**). Due to the presence of inter-individual differences, we applied a data analysis pipeline to cluster drug responses by average distances. Briefly, the distance matrix (measured by Pearson's correlation) between metaproteomic proteome content networks (PCNs)[25] was first calculated separately for each individual subject; subsequently, the distances between all compounds and controls were averaged across all subjects. Finally, K-medoids analysis revealed five clusters of drug responses (**Figure 1E**). We showed that three of the compound clusters (clusters 1, 4 and 5) deviated from the controls (**Figure 1F**). Interestingly, there appeared to be no visible correlation between the drug structure clusters in **Figure 1B** and the compound response clusters in **Figure 1E**. From the TMT-based compound response clustering, we show that across Anatomical Therapeutic Chemical (ATC) classification system level 1 classes, the proportion of compounds belonging to each K-medoids clusters are different, we therefore evaluated the enrichment of K-medoids clusters 1, 4 and 5 compounds in each ATC level 1 class. The analysis revealed no significant enrichment for any specific ATC level 1 class compared to the background of all selected compounds. However, it is still notable that Class N (targeting nervous system) showed a *p*-value of less than 0.1 (**Figure 1G**).

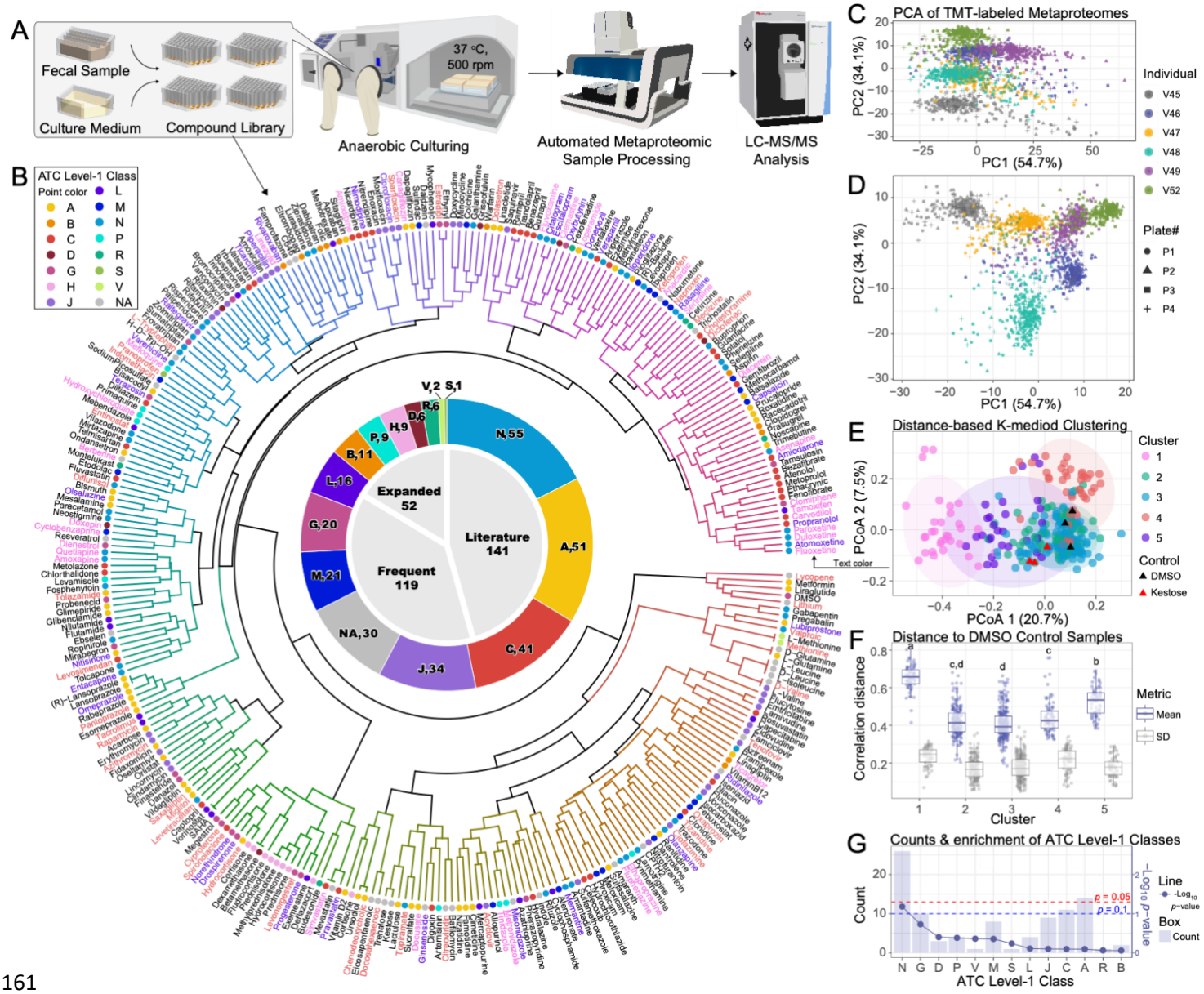

Figure 1 Screening for compounds influencing the gut metaproteome.

(A) Schematic representation of the experimental workflow. The study follows the RapidAIM 2.0 procedure[22]; fecal slurry samples of each human gut microbiota were cultured anaerobically with the presence of a compound or a control substance (DMSO or kestose). Automated metaproteomics sample processing was performed before samples are analyzed using LC-MS/MS. (B) Selection, Anatomical Therapeutic Chemical (ATC) classification and structure-based clustering of compounds in the compound library used in this study. Colors of compound labels correspond to three of the clusters in Panel E: magenta – Cluster 1, red – Cluster 4, purple – Cluster 5. (C)-(D) Principal component analysis (PCA) of all samples showing metaproteome

individuality as well as responses to compounds. (E) Distance-based K-medoids clustering of all compounds based on the average of six individual microbiome responses. Each point represents a compound or a control. Ellipses represent 95% confidence of each cluster. (F) Distance of compounds to DMSO control samples within each cluster identified in panel (D). Mean and standard deviation of the distances to DMSO control samples are shown. Letters a, b, c, and d indicate levels of significance determined by ANOVA with Tukey's posthoc test. (F) Counts of compounds corresponding to each cluster in panel (D) under different ATC level 1 classes. (G) Enrichment of various ATC level 1 drug classes in Clusters 1, 4, and 5 compounds (corresponding to the clusters identified in panel (D)), among all selected compounds.

Comprehensive profiling of metaproteomics drug responses reveals alterations in proteins and functional pathways

A total of 110 compounds from the K-medoids clusters 1, 4 and 5 (**Figure 1D** and **Supplementary Table S1**) were selected for further in-depth label-free quantification (LFQ) – based metaproteomics analysis. We used deep metagenomic sequencing of each individual microbiome sample to construct a sample-specific database for the label-free database search following the Metapro-IQ workflow[26] (**Supplementary Figure S1A**). A total of 9,326,339 LC-MS/MS spectra were identified as 195,686 unique peptides, corresponding to 36,075 unique proteinGroups. An average of 9,871 $\pm$ 3,679 peptides per sample was identified by MS/MS; in addition, 9,994 $\pm$ 2,052 proteinGroups were quantified per sample with match-between-runs option enabled during protein quantification. Label-free quantification was then performed using directLFQ[27] followed by data harmonization using HarmonizR[28]. The processed dataset thus includes over 4.6 million bacterial protein-compound responses. A series of quality-control assessment suggested high reproducibility and robustness of the whole process (**Supplementary Figure S1B-D**).

Due to this extensive spectrum of metaproteomic responses across various functional pathways and taxonomic units, it is challenging to comprehensively contain all the response figures in a single manuscript. Therefore, we have developed an interactive Shiny app as a complementary resource, available at https://shiny.imetalab.ca/MPR_Viz/. This app allows readers to select specific ATC drug classes and explore the functional and taxonomic responses of individual compounds within these classes. In more details, the app involves the responses of the individual gut microbiomes to 110 compounds selected for label-free metaproteomic quantification. Features that can be visualized involve functional annotations such as NOG categories and NOG

accessions (annotated by eggNOG mapper), KEGG KO annotations (from the KEGG database), as well as protein abundances across different taxonomic units. By providing this level of detail, the app facilitates a comprehensive exploration of the drug-microbiome interactions at both the functional and taxonomic levels. Readers can visualize data and download the figures, making it a highly informative tool for further exploration and hypothesis generation about microbiome functional responses to drugs. Here, we show an example of the Shiny app interface with an analysis result of showing several significant increases in the NOG annotation of proteins associated with efflux transmembrane transporter activity following independent treatments of several different drug from the ATC Level 1 class N (**Supplementary Figure S2**). This suggests that exposure to these drugs may have stimulated an increase in drug resistance activity, likely through the upregulation of efflux transporters.

We next examined the protein-level responses by performing the PCA of proteinGroups using the nonlinear Iterative Partial Least Squares (NIPALS) algorithm[29] within each distinct ATC class and at various ATC levels (**Figure 2**). While only a subset of compounds in each of ATC level-1 classes A (alimentary tract and metabolism), B (blood and blood forming organs), D (dermatologicals), L (antineoplastic and immunomodulating agents), and M (musculo-skeletal system) showed separation from the controls, all compounds in ATC level-1 class P (antiparasitic products, insecticides and repellents) separated from the controls on PC 1 which explains 62.7% of the variance. Classes C (cardiovascular system), G (genito urinary system and sex hormones), J (antiinfectives for systemic use) and N (nervous system) contained a larger number of compounds. We performed further explorations of PCAs on the second ATC level and presented classes that contained discriminative compounds (**Supplementary Figures S3**). On ATC level-2, we show that classes G03 (sex hormones and modulators of the genital system), J01 (antibacterials for systemic use), N04 (anti-parkinson drugs), N05 (psycholeptics) and N06 (psychoanaleptics) classes contained greater than three compounds discriminated from the controls. Among these, the ATC level-4 code N06AB (selective serotonin reuptake inhibitors) comprised six compounds with noticeable effects. By examining PCA, we observed a total of 47 compounds that are discriminative from the control in all individual microbiomes, denoted as Metaproteomics-response positive (MPR+) drugs (**Supplementary Table S2**). Among which, 39% are Class N compounds, and 15% are Class C compounds. Enrichment analysis of these 47 compounds against the background of all 312 drugs showed a significant enrichment of Class N drugs (**Supplementary Figure S4A**), suggesting that drugs targeting the nervous system have the most frequent off-target effects on gut microbes.

We were curious about which human proteins are targeted by these MPR+ compounds and whether these targets could have bacterial homologs. Therefore, by searching MPR+ compounds against the molecular drug target database by Santos et al.[30], we extracted a list of 50 human protein targets (**Supplementary Table S2**). KEGG enrichment analysis shows that these proteins are most significantly enriched in neuroactive ligand-receptor interaction and calcium signaling pathways (**Supplementary Figure S4B-C**), both are targets of Class N drugs.

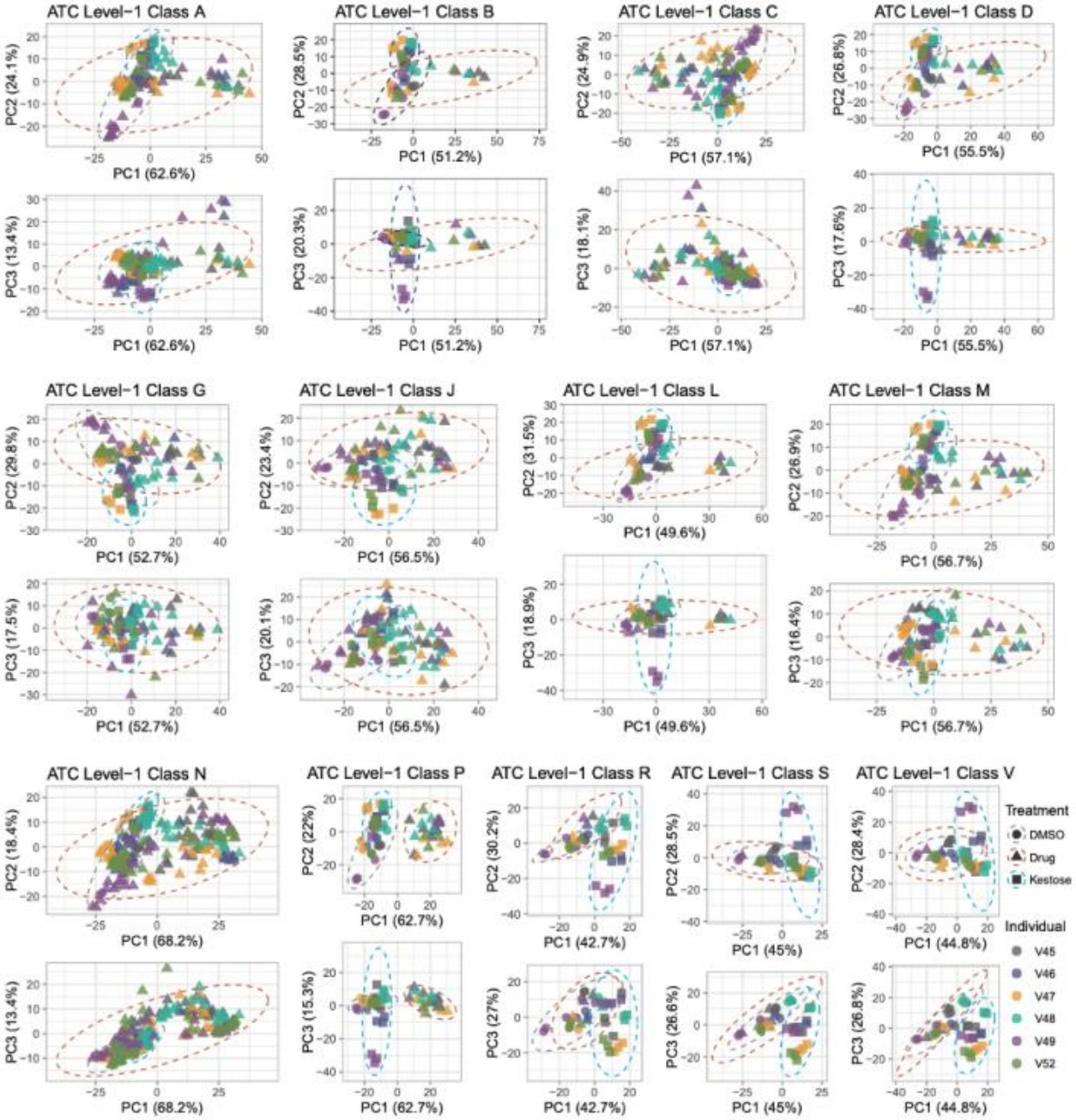

Figure 2. Overview of all individuals' gut microbiome responses across compound classes

The first three components of Principal Component Analysis (PCA) are shown. All six individual gut microbiome are shown as labeled by different colors. Gray dashed ellipse denotes 95% confidence interval of each group (red: drugs, black: DMSO and blue: kestose). Further analysis of PCA on some higher ATC level classes were shown in **Supplementary Figures S2**.

Taxonomic responses to drugs exhibit a compositional tri-stability landscape

Taxonomic responses, as it takes account into cumulative abundances of taxon-specific peptides, provides an alternative view of microbiomes community responses that is different from protein-level PCA which takes into consideration proteins as features. The compounds selected for LFQ analysis span a wide spectrum of drug structure and ATC classes. Our initial intuition was that the microbiome responses to different compounds can be highly diverse, resulting in a diverse combination of microbiome composition. To our surprise, despite observing highly diverse patterns in protein-level analysis, we identified an intriguing phenomenon in the taxonomic (genus-level) response heatmap: there's a coherent transition between three clusters of responses (**Figure 3A**). On this heatmap, microbial genera were classified into three clusters, representing three different patterns of drug responses. Among which, one cluster (Cluster 2) only included five genus-level alterations, while the two other clusters (Clusters 1 and 3) exhibited more extensive changes in 44 genera in response to 63 compounds. By color-coding different genera in each cluster with blue, orange, and green tones, the overall transition becomes apparent. This can be more easily observed by visualizing the drug response spectrum of each individual microbiome through stacked column bar plots (**Figure 3B**).

This provides evidence for the theory of multiple stability points in the microbiome[16,31], our work marks the first observation of a tri-stability landscape of individual microbiome compositions within the drug response space. To explain the phenomenon of steady states in the functional response of the microbiome to drugs, we used the generalized Lotka-Volterra (gLV) to describe the response dynamics (see **Methods**). In this model, we classified the genera observed in the experiment into three distinct clusters based on co-abundance patterns, assuming that interactions within each cluster are negligible. By adjusting the model parameters to simulate the effect of drug stimulation, we can reproduce the switches from one stable state to another (**Figure 3C**), mirroring the actual microbiome responses observed in **Figure 3B**.

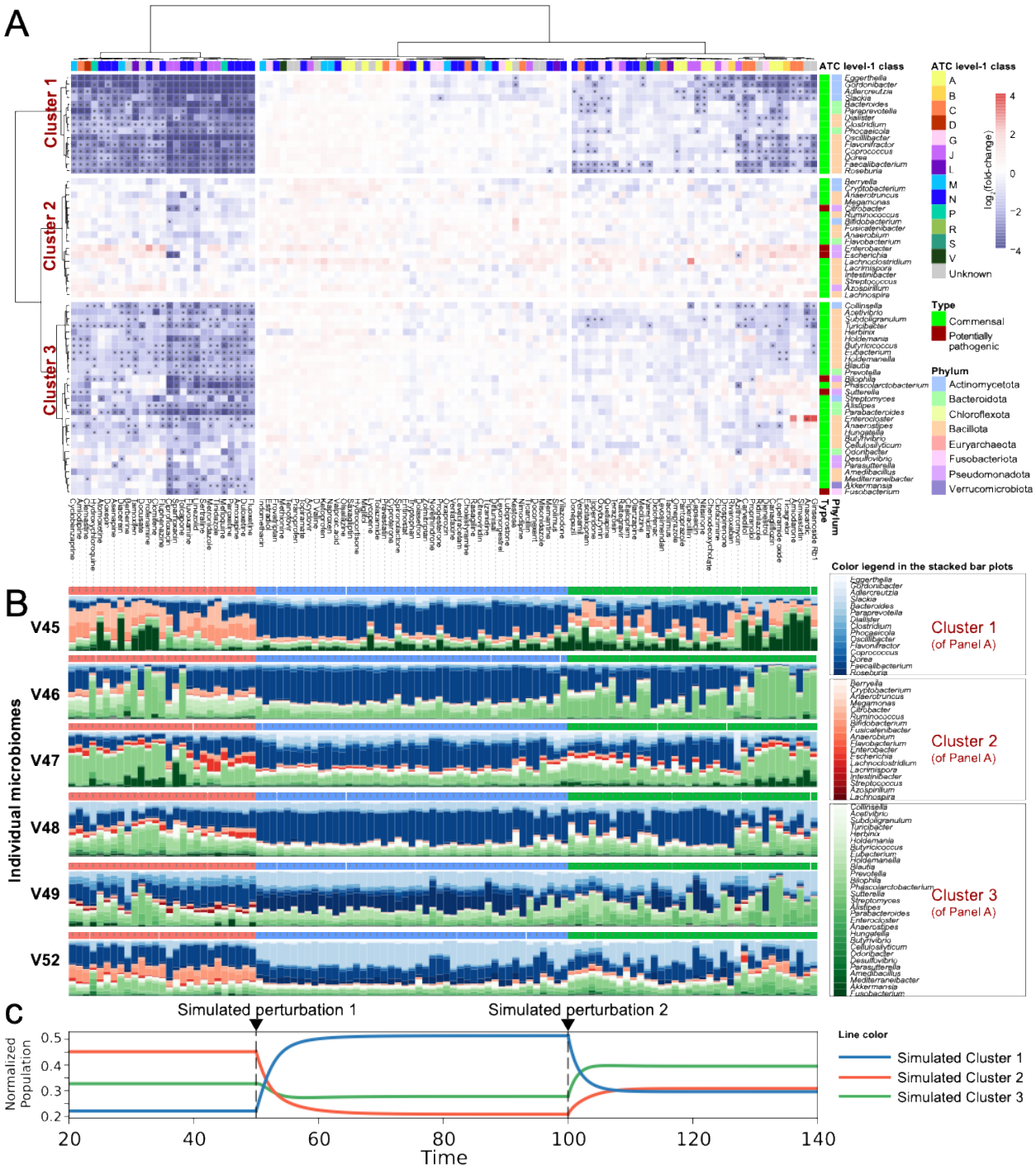

Figure 3. Taxonomic responses reveal multi-stability of individual gut microbiomes driven by drug stimulation

(**A**) Heatmap and hierarchical clustering showing log2 fold-change of overall protein biomass specific to different genera. Asterisks indicate significance levels from a two-sided Wilcoxon test,

with $P < 0.05$. (**B**) Relative abundance of genus-specific proteins presented in stacked column bar plots. The sample order agrees with panel A, and different genera are also colored according to the hierarchical clustering in panel **A**. (**C**) gLV competition model considering between-cluster interactions simulates the switches between three different stable states under drug perturbation. The time axis in panel **C** is conceptual and does not correspond to the actual order of drug treatments depicted in panels **A** and **B**.

Community state analysis reveals universal drug-specific microbial ecological responses

Examining protein and taxonomic compositions separately fails to capture the full ecological landscape from a systems perspective. Therefore, it is crucial to adopt a more ecologically relevant assessment of microbiome responses. We have previously developed a tool named PhyloFunc, which integrates phylogenetic and functional information to assess microbial community dissimilarities (i.e. beta diversity) on the ecosystem level[23]. PhyloFunc analysis was performed on each individual's microbiome including all LFQ samples of drug treatment and control conditions. The PhyloFunc distance results from different individuals were combined and visualized using Principal Coordinates Analysis (PCoA). K-means clustering was then applied, identifying three distinct community-state types (CSTs) (**Figure 4A**), with the optimal number of clusters determined as three based on the Gap statistic (**Figure 4B**). Based on these three clusters, we used a Sankey diagram to visualize the distribution of drug names and their sources across different CSTs (**Figure 4C**). Notably, all negative control (DMSO) individual microbiomes clustered into CST-3, while 41 of the compounds caused at least 80% of the tested individual microbiomes to shift into CST-1 and CST-2. These compounds include Amiodarone, Amlodipine, Amoxapine, Anacardic, Asenapine, Atomoxetine, Berberine, Canagliflozin, Carvedilol, Clemastine, Clomiphene, Cyclobenzaprine, Diacerein, Dienestrol, Docusate, Doxepin, Drospirenone, Duloxetine, Entacapone, Escitalopram, Ethoproprazine, Fluoxetine, Fluphenazine, Fluvoxamine, Ginsenoside, Hydroxychloroquine, Iloperidone, Linezolid, Loperamide, Mefloquine, Metronidazole, Oxybutynin, Paroxetine, Ridinilazole, Sertraline, Simvastatin, Tamoxifen, Ticagrelor, Tinidazole, Tolcapone, and Verapamil.

To further illustrate that PhyloFunc's inter-individual variability is not affected by individual-specific differences in protein composition, we calculated the Mean and standard deviation (SD) of PhyloFunc distances across individuals (**Figure 4D-4E**). We can clearly observe the overall

differences in heatmap intensity between the Mean and SD matrices when using the same color gradient scale. To further quantify these differences, we applied a paired Wilcoxon test on between the Mean and SD, which demonstrated a highly significant difference (p-value < 2.2e-16, N = 12,321 compound-compound interactions). Such systems-level ecological consistency in drug responses across individuals enabled us to summarize the PhyloFunc results into an averaged distance matrix (**Figure 4F**), where we identified a distinct cluster of 13 drugs, 8 of which belonged to the N-class category.

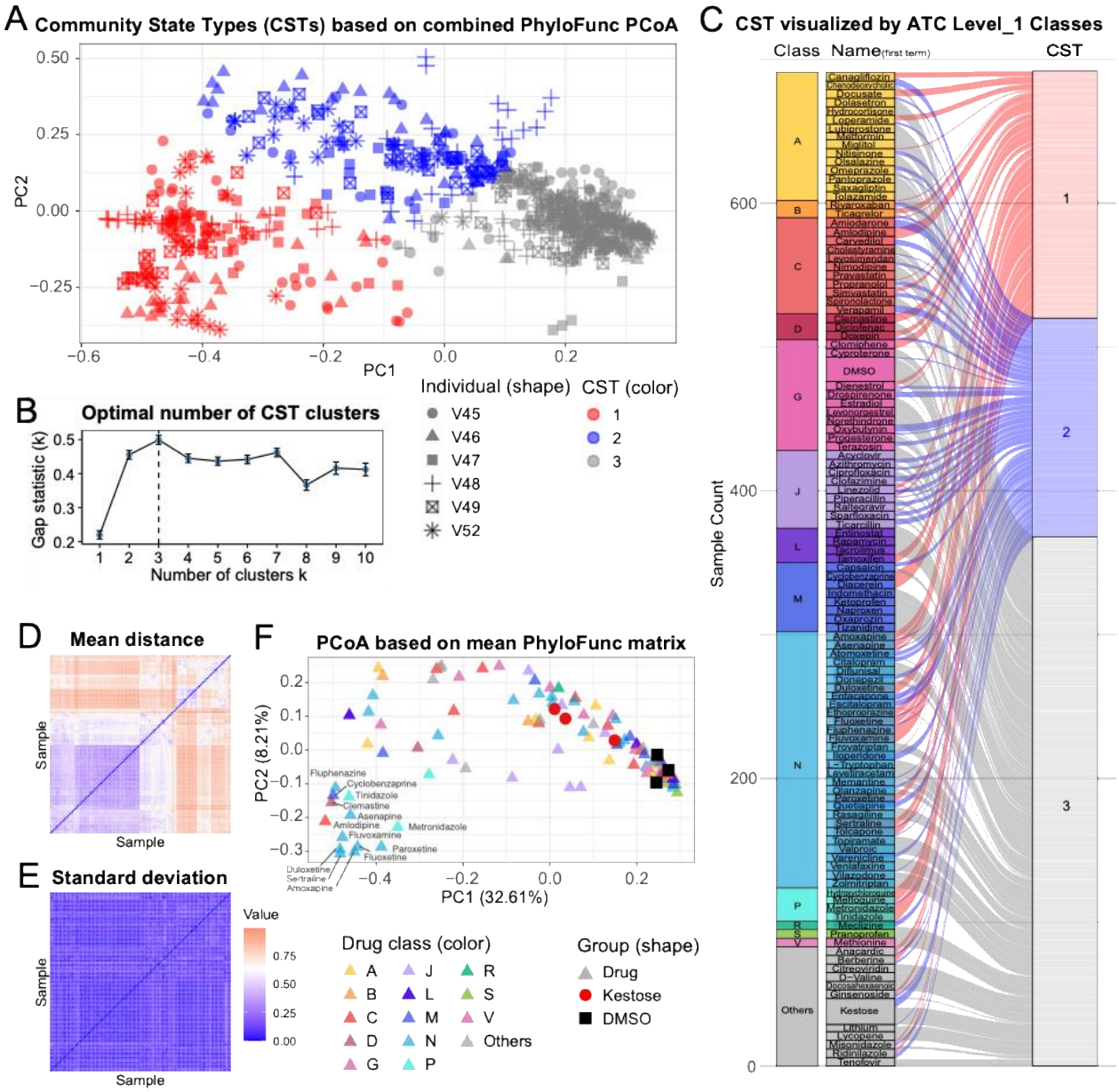

Figure 4. PlyloFunc analysis reveals impact of drugs on microbial community states.

(A) Principal Coordinates Analysis (PCoA) of PhyloFunc distances, clustering microbiome responses into three distinct Community-State Types (CSTs). (B) Determination of the optimal number of CST clusters using the Gap statistic. (C) Sankey diagram illustrating the distribution of drugs across CSTs, showing the association of compound names and their ATC level-1 classes with different CSTs. (D) Heatmap of the Mean PhyloFunc distance matrix, representing the averaged PhyloFunc distance for each compound-compound pair across individuals. (E) Heatmap of the Standard Deviation (SD) of PhyloFunc distances. (F) PCoA based on averaged PhyloFunc distance matrix across all individuals.

A subset of neuropharmaceuticals exerted similar functional effects on the ex vivo human gut microbiomes

As an example of specific interest in taxonomic and functional responses, we observed that a subset of neurological drugs exerted nearly identical effects on the human gut microbiomes as assessed by protein-level PCA, including seven drugs, namely amoxapine (ATC N06AA), **Asenapine (ATC N05AH),** duloxetine (ATC N06AX), fluoxetine (ATC N06AB), fluphenazine (ATC N05AB), fluvoxamine (ATC N06AB), paroxetine (ATC N06AB), and sertraline (ATC N06AB) (**Figure 5A**). We show that within each individual microbiome, NIPALS distances between pairs of these compounds are not significantly different compared to that between technical replicates of the DMSO and kestose control groups. In contrast, this group of compounds showed significantly higher distances from both the controls (**Figures 5B** and **5C**). Interestingly, they did not belong to a same ATC level-3/4 class, while most of these drugs are antidepressants that have been reported to have a common target of human SERT proteins, fluphenazine belongs to antipsychotics that does not target SERT. We therefore considered these drugs as a group of potentially common mode of action on the gut microbiome and visualized differentially expressed proteins of this drug group using volcano plot (**Figure 3D**). In comparison to the DMSO control group, we observed 1,447 significantly decreased proteins and 357 significantly increased proteins. By annotating the proteins to taxon (genus level) and function (COG category), we observed that the functional responses showed strong taxonomic specificity, characterised by overall decreased growth of commensals and enriched proteins of opportunistic pathogens in Pseudomonadota (**Figure 5E-5F**). Taxa having decreased functional protein classes are consistent with previous reports indicating that these taxa are also suppressed[2,32].

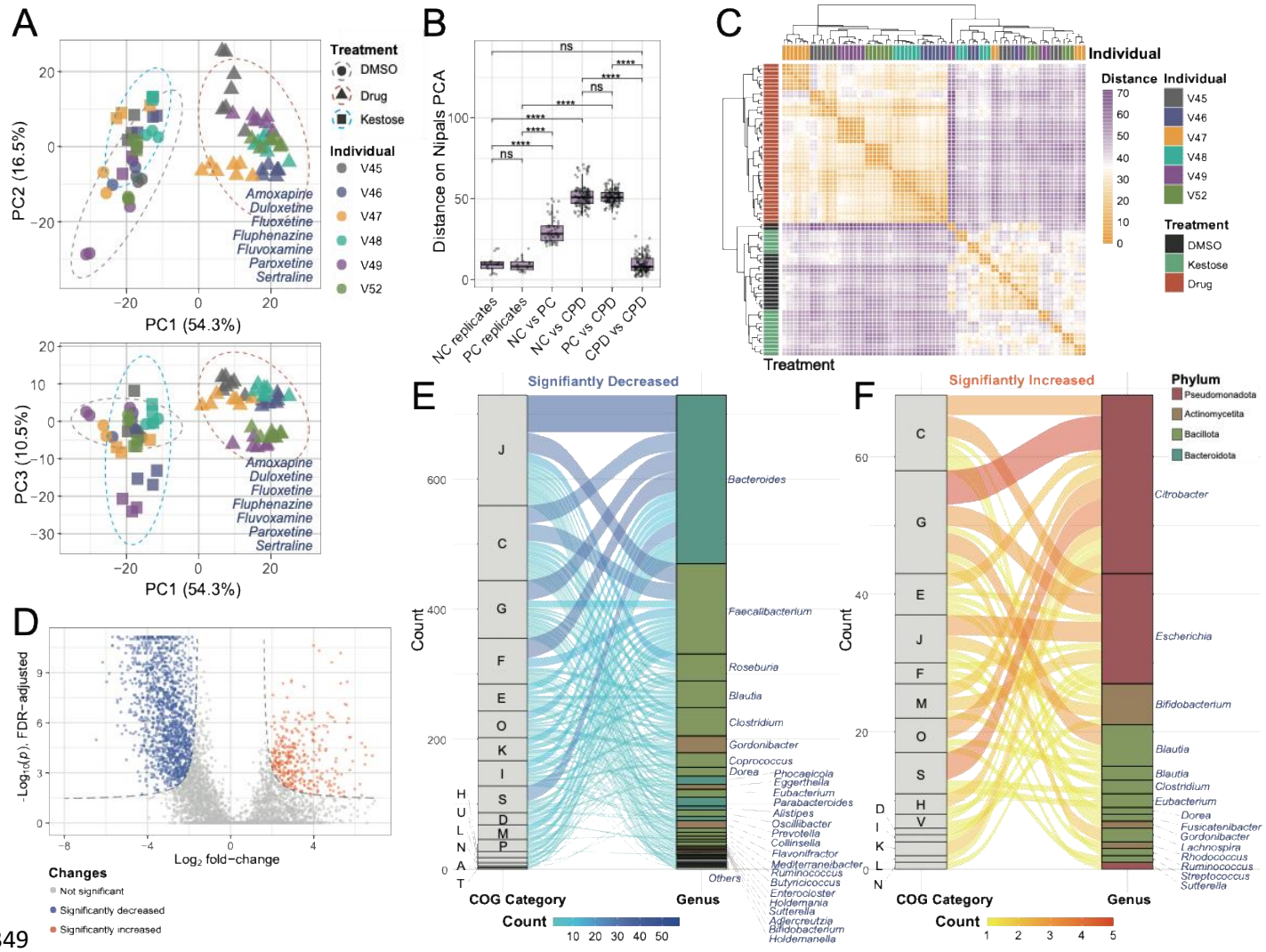

Figure 5. Seven neurological drugs showing near identical metaproteomic effects

(A) NIPALS PCA showing discriminations between the seven selected neurological drugs and the controls. (B) Between-sample distances were calculated based on NIPALS scores and the resulted distances were compared between groups. NC, negative control (DMSO); PC, positive control (kestose); CPD, seven selected compounds (C) The NIPALS score-based distance matrix was further visualized using heatmap and hierarchical clustering. (D) Volcano plot visualizing log2 fold-change of proteins versus FDR-adjusted *p* values (-log10) using a nonparametric test. Significantly differential features were determined by log2 fold-change threshold of 1.5 and adjusted *p* value of 0.05 (Wilcoxon rank-sum test). Threshold curves[33] were defined using a curvature of 1 as previously described. (E, F) Sankey plots showing taxon-specific functional responses of the significantly decreased (E) and increased (F) proteins.

Antimicrobial resistance negatively correlates to functional redundancy

We have previously performed a proof-of-concept (POC) study of the RapidAIM assay using 43 compounds, and found that drugs not only cause changes in functional and taxonomic composition, but also induce changes each individual microbiomes' levels of drug resistance proteins[4]. We further wondered whether these changes in predicted drug resistance and alteration of taxonomic composition had any relationship with a community's functional ecology properties (**Supplementary Figure S5A**). Recently, we have developed an approach to quantify a microbial community's proteome-level functional redundancy (FR_p) and its normalized version relative to the community's taxonomic diversity, nFR_p[25] (**Supplementary Figure S5B**). FR_p describes the ability of multiple taxonomically distinct organisms to contribute in similar ways to an ecosystem, providing informative insights into microbial community ecology on the functional level. Here, we first reanalyzed the RapidAIM POC dataset[4] and compared nFR_p levels with community composition and levels of antimicrobial resistance proteins (ARP) (**Supplementary Figure S5C**). We observed instances where increased prevalence of ARP occurred concurrently with a decrease in nFR_p under rifaximin (**Supplementary Figure S5D**), berberine, flucytosine, and metronidazole treatments. This case study roused our interest, and we were curious whether such phenomenon would be reproduced in this expanded collection of drug-microbiome cultures.

Hence, we analyzed the LFQ dataset using the full CARD antimicrobial resistance database[34] to redo database search and sum ARP abundance to estimate community-level drug resistance. We observed a strong negative correlation between fold-change of nFR_p and ARP ratio (Pearson's product-moment correlation coefficient *r* of – 0.695 $\pm$ 0.154, **Figure 6A**). Interestingly, nFR_p response and ARP ratio were both independent of taxonomic diversity (TD) responses (**Figures 6B and 6C)**, suggesting that antimicrobial resistance corresponds to the functional ecology status of a community, irrespective of taxonomic diversity. We also observed a mixture distribution on the scatter plot, which becomes particularly evident when performing K-medoids clustering with each individual microbiome dataset (**Figure 6D**). This suggests the presence of alternative functional states of the microbiome, wherein the microbiome can transition from its original functional ecological state of high FR_p to an alternative state of low FR_p when influenced by specific groups of compounds. We demonstrated this concept by illustrating the energy landscape of individual V45's microbiome using the Kernel Density Estimation (KDE) method

(**Figure 6E**). The upset plot demonstrates a high level of common presence of these compounds across each individual microbiome's high FR_p clusters (**Figure 6F**). We calculated the frequency of compounds in the high FR_p clusters by summing their occurrences across all individual datasets, N05A (antipsychotics) and N06A (antidepressants) drug classes of ATC level 3 showed a high frequency of appearance in the high FR_p clusters compared to other N class drugs targeting the neural system (**Figures 6G-H**).

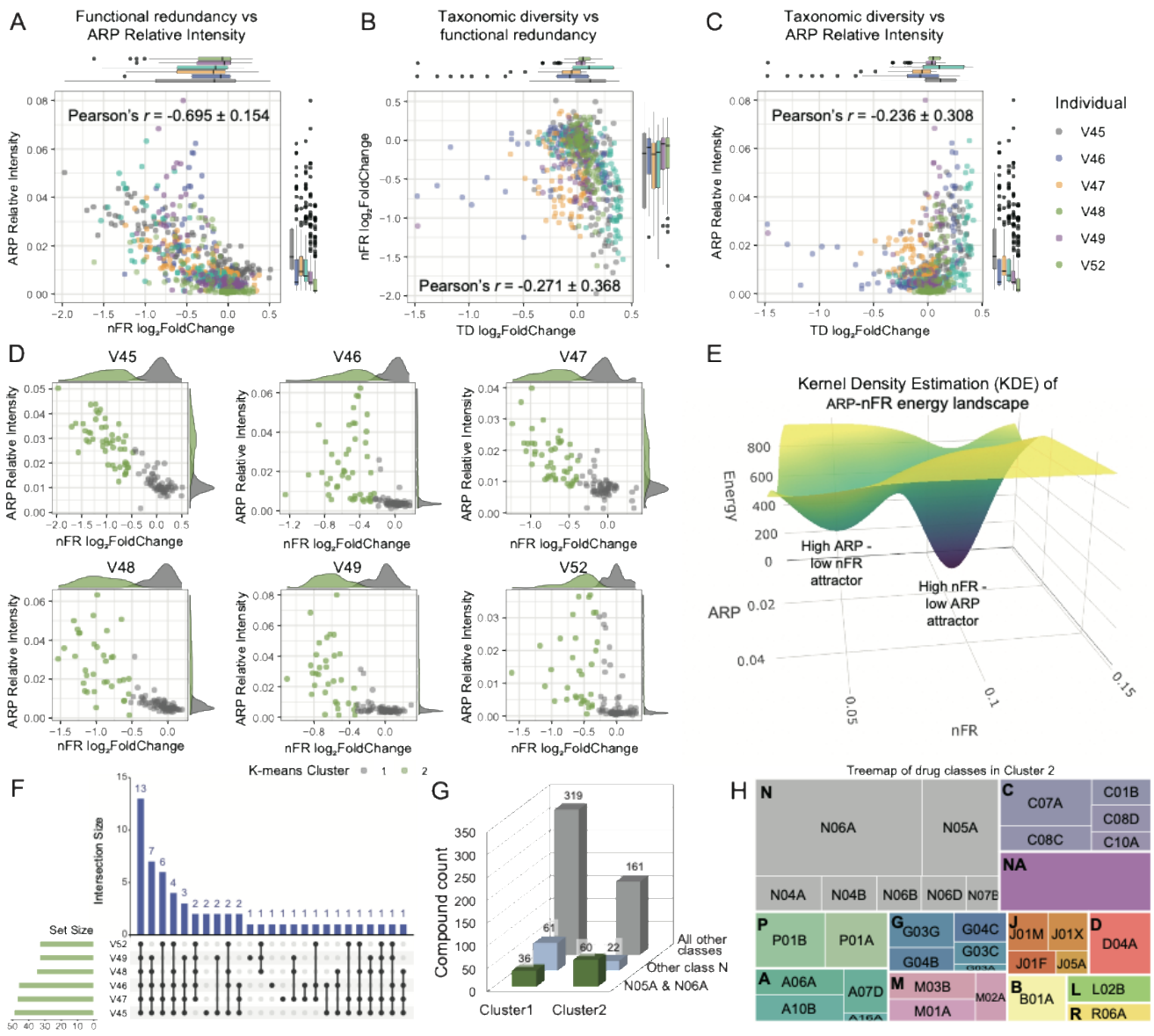

Figure 6. ARP abundance negatively correlates with functional redundancy

(A) Scatter plot and Pearson's correlation between functional redundancy log2 fold-change and ARP ratio. (B) Scatter plot and Pearson's correlation between taxonomic diversity log2 fold-change and functional redundancy log2 fold-change. (C) Scatter plot and Pearson's correlation between taxonomic diversity log2 fold-change and ARP ratio. In panels (A)-(C), box plots show value distributions based on individual microbiome corresponding to each axis. The thicker black line in the box plot denotes median, the lower and upper hinges correspond to the first and third quartiles, the box ranges from the 1.5 × (interquartile range) below the lower hinge to 1.5 × IQR above the upper hinge, and whiskers represent the maximum and minimum values, excluding outliers. D) K-medoids clustering of ARP-FR response by individual. (E) Energy landscape of ARP-nFR_p response by KDE method. (F) Set comparison of Cluster 2 compounds across individuals. (G) Counts of Cluster 1 & 2 compound frequencies in different classes. (H) Tree map showing frequency of occurrence in Cluster 2. Bold capital letters indicate ATC level 1 classes, and capital letters with numbers indicate ATC level 3 classes.

Enhanced functional redundancy mitigated drug-induced ARP

Considering the ARP-nFR_p drug response energy landscape shown in **Figure 6E**, and based on the dynamic mechanisms of energy landscapes, we wondered if functional redundancy could be leveraged to prevent drug-induced shifts of the microbiome's functional state from the high nFR_p-low ARP attractor to the high ARP-low nFR_p attractor. Specifically, our hypothesis was that while a microbiome was stimulated by an ARP-inducing drug (for example, cluster 2 drugs), adding another compound that can increase a microbiome's functional redundancy may help combat the functional redundancy decline and suppress ARP. To test this hypothesis, we designed a 2x2 factorial design as shown in **Figure 7A**.

We selected sertraline as our model for an ARP-inducing drug, as it showed the strongest effect in reducing nFR_p and increasing ARP levels across all six individual microbiomes (**Supplementary Figure S6A**). Sertraline was also shown to be pathogen-favoring in previous research[35]. Fructooligosaccharide (FOS) was selected as a nFR_p enhancing compound because it increased nFR_p in a subset of previously tested individual microbiomes[4] (an example is shown in **Supplementary Figure S5C**). Since the nFR_p response to FOS can vary between individuals, we performed a pretest using three additional individual microbiomes and selected one microbiome with the highest level of nFR_p increase in the presence of FOS (**Figure 7B**) and performed the 2x2 factorial design experiment**.** The effects of the different combinations on

nFR_p and ARP are measured using metaproteomics. Results show that sertraline alone decreased nFR and increased ARP (first group of comparisons in **Figure 7C and D**). When sertraline was combined with FOS, it did not decrease nFR nor increase ARP, as compared to the microbiome treated by FOS alone (second group of comparisons in **Figure 7C and D**). Furthermore, compared to the microbiome treated only with sertraline, those treated with both sertraline and FOS showed significantly increased nFR_p and decreased ARP (third group of comparison in **Figure 7C and D**). In addition, sertraline increased the abundance of Enterobacterales, but this increase did not occur when sertraline was present alongside FOS (**Supplementary Figure S6B**). These findings together suggest that manipulating the microbiome to increase nFR_p could potentially counteract the increase in ARP and help maintain microbiome resilience against drug-induced negative impacts.

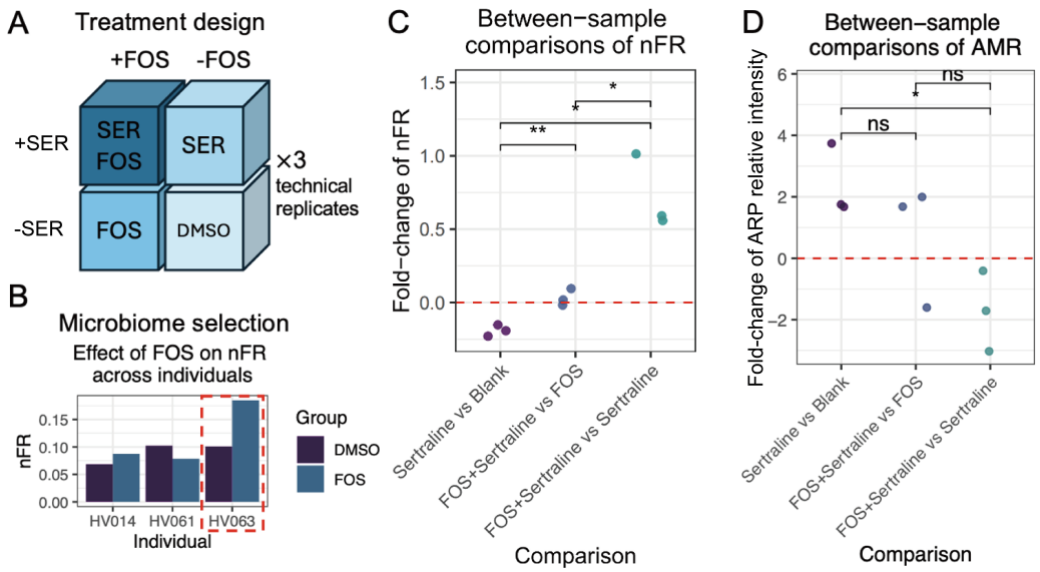

Figure 7. Functional redundancy acts as a potential target to combat drug-induced ARP

(A) Experimental design, sertraline was abbreviated as SER on the figure. (B) Pretest of individual gut microbiome responses to FOS show individualized nFR_p alterations. (C) Between-sample comparisons of nFR_p and (D) ARP.

DISCUSSION

In this study, we screened 312 commonly prescribed and structurally diverse drugs and compounds against *ex vivo* human gut microbiotas using the RapidAIM 2.0 approach and selected a subset of 110 drugs to quantitively reveal their metaproteomic responses, which are presented in an interactive Shiny app as a useful resource for the resource community. We performed functional and ecological analyses of the metaproteomes across three hierarchical levels: protein-level, taxonomic composition-level, and systems ecological-level.

On the protein level, we discovered that ATC 1st level drug classes C (cardiovascular system), G (genitourinary system and sex hormones), J (anti-infectives for systemic use), and N (nervous system) exhibited the most observations of deviated metaproteomics from the controls in our non-supervised multivariate analysis. Among these, class N was a class that showed significant enrichment drug category that induced metaproteomic changes compared to the entire drug list of this study. We summarised 47 MPR+ drugs based on the protein-level responses. Further analysis on the 47 MPR+ drugs' protein targets suggest a potential link between human protein targets and microbial drug responses, indicating that microbial communities may be influenced by drugs through interactions with homologous bacterial proteins. The significant enrichment of human drug targets in neuroactive ligand-receptor interactions and calcium signaling pathways among the list of 47 MPR+ drugs' human targets raise the possibility that certain microbial responses to drugs could be mediated by unintended interactions between drugs and bacterial homologs of human protein targets, potentially influencing microbiome composition and function. For instance, selective serotonin reuptake inhibitors (SSRIs) and serotonin-norepinephrine reuptake inhibitors (SNRIs), commonly used for treating depression, target human neurotransmitter sodium symporters (NSS) including human serotonin transporter (SERT)[30,32] responsible for serotonin reuptake. Further studies could explore the extent to which drugs contribute to unintended pharmacological effects through molecular-level interactions with microbial protein targets.

We next explored the ecological responses at the taxonomic composition level. Counterintuitively, the microbial community composition did not exhibit a broad continuum of distributions but instead formed three distinct states, suggesting the universal presence of multi-stability in microbial communities across their drug response landscape. To further investigate the theoretical principles underlying this tri-stability, we applied the generalized Lotka-Volterra (gLV)

model to describe the response dynamics and understand the stability of microbial community states. However, we acknowledge that our current model is theoretical and may oversimplify the actual microbiome dynamics. Specifically, it does not account for the continuous transitions between states observed in individual microbiota. Future work can focus on determining the actual model parameters by time-series experimental observations. A highly descriptive model of the individual microbiome behavior under various interventions will enable the development of personalized medicine and modulation of the microbiome.

Neither protein-level nor taxonomic unit-level analyses can truly reveal the ecological system-level landscape of a gut microbiome's drug responses. We've previously developed PhyloFunc and demonstrated its strength in revealing underlying ecological-level functionality differences between communities, by leveraging phylogenetic trees to weigh functional distances between samples on each taxon's nodes. Unlike protein-level PCA, which utilizes HarmonizR to remove inter-individual differences in protein abundance distribution (via its built-in Combat algorithm) to enhance the detection of consistent responses, PhyloFunc captures ecosystem diversity directly from the original protein group data without requiring data harmonization across individuals. This indicates that drug responses at the ecosystem level are inherently more consistent across individuals, which cannot be fully captured at the taxonomic or protein level alone due to inter-individual variability in species composition. PhyloFunc mitigates such variability by reducing ecosystem differences introduced by protein abundance variations among phylogenetically similar species, thereby providing a more ecologically meaningful perspective. Our finding suggests that while metagenomics and metaproteomics have long been used to reveal inter-individual microbiome diversities in strains, genes, and proteins, a striking level of consistency emerges at the functional ecosystem level.

Notably, in all different levels of response landscapes, we observed that several drugs targeting the nervous system - amoxapine, duloxetine, fluoxetine, fluphenazine, fluvoxamine, paroxetine, and sertraline – were identified with strong effects on microbial proteins and community ecology, characterized by an overall decrease in the growth of commensals and an enrichment of pathogen-associated proteins. Such negative effects should be modulated to prevent long-term drug use from causing damage to gut health. However, the high species compositional complexity of the microbiome can lead to off-target drug effects across multiple microbial species, making it unlikely to pinpoint a universal gut species as a target to mitigate drug effects. Innovatively, we discovered an approach to combat a drug's off-target effects by leveraging the functional ecological landscape of the microbiome. Antimicrobial resistance protein (ARP)

analysis showed that microbiome-level resistance to nonantibiotic compounds is widespread, and it is associated with compromised community stability and resilience. We further observed a functional bi-stability, which is characterized by an alternation between high functional redundancy (FR_p) community with low ARP, and low FR_p with high ARP status. Assuming state shifts between functional attractors, we explored strategies to counteract sertraline-induced increases in ARP by leveraging the ecosystem-level property of FR_p[25]. We show that by using prebiotic FOS, the ecosystem can potentially buffer against the functional redundancy loss in specific individual microbiomes and prevent the system from shifting to an undesirable state dominated by resistant strains. Our study highlights the great potential of personalized microbial systems ecology strategy by utilizing the functional landscape to mitigate undesirable off-target drug responses in human gut microbiota.

METHODS

Key resources table

REAGENT or RESOURCE	SOURCE	DENTIFIER
RapidAIM 2.0 Assay – Microbiota culturing		
Potassium phosphate monobasic	Millipore-Sigma - Sigma-Aldrich	P5655
Potassium phosphate dibasic	Millipore-Sigma - Supelco	PX1570-1
Sodium chloride	Calbiochem - OmniPur®	7710
Magnesium sulfate heptahydrate	Millipore-Sigma - Sigma-Aldrich	230391
Calcium chloride, anhydrous	Millipore-Sigma - Sigma-Aldrich	C5670
Tween® 80	Millipore-Sigma - Sigma-Aldrich	P4780
Sodium cholate hydrate	Millipore-Sigma - Sigma-Aldrich	C9282
Sodium chenodeoxycholate	Millipore-Sigma - Sigma-Aldrich	C8261
Peptone water	Millipore-Sigma - Sigma-Aldrich	70179
Bacto™ yeast extract	Becton, Dickinson and Company	212750
Sodium bicarbonate	Millipore-Sigma - Supelco	SX0320
L-cysteine	Millipore-Sigma - Sigma-Aldrich	C7352
1-Kestose	TCI America	K0032
Hydrochloric acid	Fisher Chemical	A144S
RapidAIM 2.0 Assay – Metaproteomic sample processing		
Phosphate buffered saline, 10X solution	Fisher BioReagents	BP399-4
Urea	Millipore-Sigma - Sigma-Aldrich	U5378
Tris (hydroxymethyl)aminomethane	Calbiochem - OmniPur®	9230
Sodium dodecyl sulfate	Millipore-Sigma - Sigma-Aldrich	L3771
Acetone	Millipore-Sigma - Sigma-Aldrich	179124
Acetic acid, glacial	Fisher Chemical	A38-212
Acetonitrile	Millipore-Sigma - Sigma-Aldrich	34851
Ethyl alcohol, anhydrous	Commercial Alcohols	P016EAAN
Formic acid	Millipore-Sigma - Sigma-Aldrich	F0507
cOmplete™ protease inhibitor cocktail	Millipore-Sigma - Roche	04693116001
Dithiothreitol	Millipore-Sigma - Sigma-Aldrich	43815

Iodoacetamide	Millipore-Sigma - Sigma-Aldrich	I1149
Trypsin	Worthington Biochemical	L5003740
DC Protein Assay Reagents A, B and S	Bio-Rad Laboratories	5000113, 5000114 and 5000115
RapidAIM 2.0 Assay – TMT labelling		
TMT10plex Isobaric Label Reagent Set plus TMT11-131C Label Reagent	Thermo Scientific	A34808
50% hydroxylamine (HOA) for TMT experiments	Thermo Scientific	90115
1M triethylammonium bicarbonate (TEAB) for TMT experiments	Thermo Scientific	90114
Pierce™ quantitative colorimetric peptide assay	Sigma-Aldrich	23275
RapidAIM 2.0 Assay – Consumables		
Culture plate	Sigma-Aldrich	CLS3960
Culture plate lid	Thermo Scientific	AXYAM2MLSQ
Lysis plate	Thermo Scientific	AB-0600
Lysis plate lid	Sigma-Aldrich	AB-0783
Precipitation plate	Sigma-Aldrich	CLS4413
Precipitation plate lid	Thermo Scientific	CLS4418
Elution plate	Thermo Scientific	AB-0859
Elution plate lid	Thermo Scientific	278616
TMT plate	Thermo Scientific	249944
TMT plate lid	Axygen™	276002
Reservoir	Eppendorf	RESSW96HP
RapidAIM 2.0 Assay – Automation		
Automated 96-channel liquid handling platform	Hamilton	OPP041219
Desalting tip columns	IMCS	04T-H6R05-1-10-96
RapidAIM 2.0 Assay – LC-MS/MS Analysis		
UltiMate 3000 RSLCnano system	Thermo Fisher Scientific	ULTIM3000RSLCNANO
Orbitrap Exploris 480 mass spectrometer	Thermo Fisher Scientific	BRE725533
Metagenomic Analysis		
FastDNA Spin Kit	MP Biomedicals	116540600
Qubit High Sensitivity dsDNA Assay Kit	Thermo Fisher Scientific	Q32851
Illumina NovaSeq 6000	Illumina	NovaSeq 6000
Software and bioinformatic tools		
MetaLab	https://imetalab.ca	Version 2.3.0
MaxQuant	https://www.maxquant.org/	1.5.2.8
X!Tandem	https://www.thegpm.org/TANDEM/	Version 2015.12.15.2
directLFQ[27]	https://github.com/MannLabs/directlfq	MacOS version 0.2.8
eggNOG mapper	http://eggnog-mapper.embl.de/	Version 2.1.12
fastp	https://github.com/OpenGene/fastp	Version 0.23.1
Kraken2	https://github.com/DerrickWood/kraken2	Version 2.1.2
Genome Reference Consortium Human Build 38	Genome Reference Consortium	GRCh38hg38
phiX reference genomes	NCBI	phiX174
bbcms	BBMap suite	Version 38.34
MEGAHIT	https://github.com/voutcn/megahit	Version 1.2.9
Prodigal	https://github.com/hyattpd/Prodigal	Version 2.6.3
R	R Foundation	Version 4.0.4

Sample collection and biobanking

The protocol for human stool sample collection (# 20160585–01 H) was approved by the Ottawa Health Science Network Research Ethics Board at the Ottawa Hospital, Ottawa, Canada. The inclusion criteria of participants were 18-65 years of age and healthy. Exclusion criteria included diagnosis of irritable bowel syndrome, inflammatory bowel disease, or diabetes; antibiotic use or gastroenteritis episode three months preceding collection; use of pro-/pre-biotics, laxatives, or anti-diarrheal drugs in the last month preceding collection; or pregnancy. Six individual microbiomes were collected and biobanked according to our previously validated workflow[20]. Briefly, fecal samples were collected off-site from participants using a provided sample collection kit. Participants collected their samples with a commode specimen collection system and a sterile scoop, transferring the sample to a labeled, leak-proof Falcon tube. After adding a deoxygenated feces stabilization buffer (1X phosphate buffered saline with 10% (v/v) glycerol and 1 mg/mL L-cysteine), the samples were sealed in biohazard transport bags with absorbent material and cold packs. The sealed packages were shipped back to the laboratory in insulated boxes to maintain the appropriate temperature, ensuring sample integrity during transport. Fecal samples were weighed in lab, and additional stabilization buffer was added to make a 20% (w/v) fecal concentration. Final fecal slurry was made in an anaerobic chamber by vortexing with the addition of glass beads, and gauze filtering. Samples were aliquoted in 15 mL Falcon tubes and stored at -80 °C until culturing. We have previously validated that the live microbiota biobanking approach can reproduce the metaproteomic responses of fresh stool samples[20].

RapidAIM 2.0 assay

Drug plate preparation: For quality control (QC), each plate included triplicate wells for DMSO (negative control) and triplicate wells for kestose (positive control). Blank wells contained only media and were not inoculated; they were designed to be tested for protein concentration to confirm the absence of contamination. Information of the tested compounds is given in **Supplementary Table S1**. For most compounds, 10 mM stocks in DMSO were made. For compounds without exact molecular weights (e.g. mixtures of polymers), 1 mg/ml stocks were prepared. For compounds dissolvable in ddH_2O but not in DMSO, the stocks were prepared in ddH_2O. RapidAIM 2.0 assay plates were next prepared by adding 50 µL of each stock solution in the well designated to the specific compound to achieve 500 µM (or 50 µg/mL for compounds without exact molecular weights) concentration in the final culture system. Compounds were distributed randomly across four plates. For negative control wells, 50 µL of DMSO was used. For compound stocks prepared with ddH_2O, 50 µL of DMSO was added to control the DMSO effect.

The plates were stored at -20 °C before the culturing experiment following RapidAIM 2.0 workflow.

Microbiome culturing and drug treatment: Culture media was optimized and validated in our previous study[36], which includes the following composition: 2.0 g/L peptone water, 2.0 g/L yeast extract, 0.5 g/L L-cysteine hydrochloride, 2 mL/L Tween 80, 5 mg/L hemin, 10 µL/L vitamin K1, 1.0 g/L NaCl, 0.4 g/L K_2HPO_4, 0.4 g/L KH_2PO_4, 0.1 g/L $MgSO_4 \cdot 7H_2O$, 0.1 g/L $CaCl_2 \cdot 2H_2O$, 4.0 g/L $NaHCO_3$, 4.0 g/L porcine gastric mucin, 0.25 g/L sodium cholate and 0.25 g/L sodium chenodeoxycholate. RapidAIM 2.0 culturing experiments were performed in an anaerobic chamber whose gas contained 5% H_2, 5% CO_2 and 90% N_2. The drug plate containing 50 µL DMSO and a compound in each treatment well was added with 1 mL culture media and 100 µL fecal slurries as inoculum. Samples were mixed sufficiently using multi-channel pipettes before covering the wells tightly with a perforated silicone gel mat and sealed around using lab tape to prevent popping up due to gas production in the culture. The deepwell plates were shaken at 500 rpm on an orbital shaker for 48 hours at 37 °C.

Microbial cell washing: After culturing, culture plates were centrifuged at 3,000 g for 45 minutes at 4 °C to collect the microbial cells. The cell pellets were then washed three times with 1 mL of cold PBS. In the final wash cycle, the pellets were resuspended in an additional 1 mL of cold PBS and briefly centrifuged at 300 g for 5 minutes at 4 °C to clear debris. The resulting supernatant was carefully transferred to a new deep well plate and subjected to a final centrifugation at 3,000 g for 45 minutes at 4 °C. The purified cell pellets were subsequently stored at -80 °C until needed for cell lysis.

Microbial cell lysis and protein double-precipitation: Proteins were then extracted from the cells using ultra-sonication and were purified using a double-precipitation procedure. Initially, microbial cell pellets were lysed with 150 µL of lysis buffer (8 M urea and 4% sodium dodecyl sulfate (SDS) in 100 mM Tris-HCl, pH = 8.0) per well using a 96-channel liquid handler. The lysates underwent sonication using Qsonica Q700 at 10 kHz, alternating 10 seconds on and 10 seconds off for a total of 10 minutes, with cooling at 8 °C to prevent overheating. The sonicated lysates were transferred to a cluster tube plate and mixed with 800 µL of ice-cold protein precipitation solution (50%:50%:0.1% (v:v:v) of acetone:ethanol:acetic acid), then precipitated overnight at -20 °C. Following the first precipitation, the sample plates were centrifuged at 3,000 g, 45 min, 4 ^{o}C, and the supernatant was discarded. The pellets were then resuspended in 150 µL of protein resuspension buffer (6 M urea in 100 mM Tris-HCl, pH = 8.0) and subjected to a second precipitation under the same condition.

Protein digestion: Protein concentrations of the DMSO control samples were measured using the DC Protein Assay kit according to the manufacturer's instructions. An equal volume approach was applied similar to described previously[4]: DMSO control samples were diluted to 1 µg/µL with the resuspension buffer (6 M urea in 100 mM Tris-HCl, pH 8), and the same volume of the resuspension buffer was added to other sample wells. Protein digestion was next performed using an automated liquid handler (Hamilton Nimbus 96): each well received 10 µL of 0.1 M dithiothreitol (DTT) solution for reduction at 56°C for 30 minutes; after cooling, 10 µL of 0.2 M iodoacetamide (IAA) solution was added for alkylation in the dark at room temperature for 40 minutes; finally, 1000 µL of 1 M Tris-HCl buffer with 2 µg/mL trypsin (enzyme-to-protein ratio 1:50) was added, and the samples were incubated at 37°C overnight.

Protein desalting and TMT labelling: After digestion, desalting of protein lysate was performed using the same automated liquid handler using reverse-phase (RP) desalting columns (IMCS, 04T-H6R05-1-10-96). A 240 µL aliquot of the 800 µL desalting elute was used for 96-well format TMT 11plex™-labeling following an economic and robust approach that was previously described[21]. Briefly, 11 different tandem mass tags (TMT) reagents are first resuspended in acetonitrile, aliquoted into precise 50 µg TMT per channel, freeze-dried, and stored at -80 °C. For peptide labeling, the peptide aliquots (dissolved in 100 mM TEAB with 20% acetonitrile) are added to each well of a pre-prepared TMT plate, thoroughly mixed, and incubated at 25 °C for 1-2 hours. Post-incubation, the reaction is quenched, and the pH adjusted to 2-3. Finally, the labeled peptides are combined, desalted, and freeze-dried for further analysis. TMT labeled samples were desalted and dried in a SpeedVac at room temperature.

LC-MS/MS analysis

TMT-labelled samples: LC-MS/MS analyses of TMT-labeled samples were performed using an UltiMate 3000 RSLCnano system coupled to an Orbitrap Exploris 480 mass spectrometer (ThermoFisher Scientific Inc.). Peptides were separated using a 75 µm × 50 cm analytical column packed with reverse phase beads (1.9 µm/120-Å ReproSil-Pur C18 resin, Dr. Maisch HPLC GmbH), applying a two-hour gradient from 5%~35% of buffer B (0.1% (v/v) formic acid with 80% (v/v) acetonitrile) ratio with buffer A being 0.1% formic acid, at a flow rate of 300 nL/min. Full MS scans were acquired in the Orbitrap at a resolution of 120,000 for 350-1,200 m/z. Data were acquired in a data-dependent mode with a cycle time of 2 seconds between master scans. MS/MS scans were performed using higher-energy collisional dissociation (HCD) at a resolution of 45,000, with a collision energy of 30%. The dynamic exclusion was set to 60 seconds after a single count.

Label-free samples: LC-MS/MS analyses of label-free samples were also performed using the UltiMate 3000 RSLCnano and the Orbitrap Exploris 480. Peptides were separated using a tip column (75 µm inner diameter × 15 cm) packed with reverse phase beads (3 µm/120 Å ReproSil-Pur C18 resin, Dr. Maisch HPLC GmbH), applying a one-hour gradient from 5%~ 35% of buffer B (0.1% (v/v) formic acid with 80% (v/v) acetonitrile) ratio, with buffer A being 0.1% formic acid, at a flow rate of 300 nL/min. Full MS scans were acquired in the Orbitrap at a resolution of 60,000 for 350-1,200 m/z by data-dependent MS/MS scan of the 15 most intense ions. MS/MS scans were performed using higher-energy collisional dissociation (HCD) at a resolution of 15,000, with a collision energy of 30%. The dynamic exclusion repeat count was set to one, and the repeat exclusion duration was set to 20 seconds.

Metagenomics analysis

Fecal slurries of different individual microbiomes were first subjected to whole metagenomic DNA extraction using the FastDNA Spin Kit (MP Biomedicals, 116540600). Quantification of DNA contents was performed using the Qubit High Sensitivity dsDNA Assay Kit, as previously described[37]. Metagenomic DNA sequencing was performed with Illumina NovaSeq 6000 platform at Génome Québec CES using PCR-free library preparation. A total of 2.58B reads were sequenced for six samples with an average of 430M (±70M) per individual microbiome. The generated fastq sequences were preprocessed using fastp v.0.23.1[38] to remove adaptors and quality filter the reads with default parameters. Human and phiX reads were then removed by mapping the reads to a non-redundant version of the Genome Reference Consortium Human Build 38 (GRCh38hg38; RefSeq: GCF_000001405.39) and phiX reference genomes using the Kraken2 v.2.1.2 package[39]. The quality-filtered paired-end reads were then error-corrected using bbcms v38.34 from the BBTools[40] with default parameters. An average of 420M (±69M) reads were obtained after these steps. Metagenome assembly of the error-corrected and quality-filtered non-human reads was performed using MEGAHIT v1.2.9[41] using the --presets meta-large --min-contig-len 1000 parameters. A total of 640,099 contigs with lengths >1,000 bp were individually assembled, with an average of 106,683 (±32,133) contigs per individual microbiome. The assembled contigs were then annotated using the PROkaryotic Dynamic programming Gene-finding ALgorithm (Prodigal) v2.6.3[42] to predict open reading frames (ORF). The contigs were translated into amino acid sequences using the anonymous gene prediction mode (prodigal -p meta) and default parameters and annotated a total of 3.8M protein-coding genes. Lastly, the

outputs were compiled into a single FASTA file and used as the metagenome-inferred protein database for the metaproteomic search.

Database search strategy

The initial TMT dataset's database search aimed for the screening of compounds for in-depth LFQ analysis was performed using MetaLab (Version 2.3.0)[43] with the IGC database[44] as the reference database. Following LFQ analysis, we established a bioinformatic workflow for sample set specific database generation. Briefly, metagenomic prodigal sequences (in FASTA format) from each individual microbiome were used to construct reduced databases of each subset of individual microbiome's LFQ LC-MS/MS raw files following the MetaPro-IQ workflow[26]. Databases reduced from two-step X!Tandem search based on individual raw file subsets were merged and subjected to redundancy removal at 99% using CD-HIT. The resulting FASTA file containing 491,506 FASTA sequences was used for database search of LC-MS/MS label-free files using MaxQuant (version 1.5.2.8), as well as revisiting the TMT dataset's database search using MaxQuant (version 2.0.3.0). Both LFQ and TMT searches applied carbamidomethylation as a fixed modification (C) and variable modifications including acetylation at the protein N-terminus and oxidation of methionine, with a fragment ion tolerance of 20 ppm. The false discovery rates (FDR) for peptide spectrum matches (PSM) and proteins were set to 0.01, with a minimum peptide length of 7. Match between runs were enabled with matching time window of 0.7 minutes and alignment time window of 20 minutes. Database search of ARP was performed using the full CARD database[34] (downloaded December 27th, 2022) in MaxQuant 1.5.2.8, using the same search parameters as above.

Data preprocessing

For the TMT dataset, proteinGroup.txt was normalized using MSstatsTMT[45] with the "msstats" option selected, and perform estimate size factors on matrix using Deseq2 R package, the processing resulted in 19,318 proteinGroups across all TMT samples. A Q15 criteria was applied to remove highly random sparse features, and SpectroFM was applied for data imputation, resulting in a matrix of 6085 proteinGroups.
For the LFQ dataset, directLFQ[27] (GUI MacOS version 0.2.8) was used for efficient label-free quantification, followed by protein inference using a custom in-house script (available at https://github.com/ningzhibin/protein-Inference). Razor and unique peptides were considered for protein quantification. Dataset was further harmonized by individual microbiome batch using the

R package HarmonizR[28], which implements the ComBat algorithm while appropriately handling missing values[28].

For the ARP database search result, protein intensities in the proteinGroups file were filtered to remove potential contaminants and reverse sequences, then all protein intensities in each sample were summed as ARP intensities. The ARP ratio in each sample was then calculated by dividing the ARP intensities by the total protein intensities in the LFQ search result.

Taxonomic and functional annotation

Taxonomic annotation was performed in MetaLab 2.3.0[43] by searching the peptide sequences against the pep2taxa database in MetaLab. Taxonomic annotations with three or more unique peptides were considered confident, following the conservative criteria used in previous studies[43,46]. eggNOG mapper (version 2.1.12)[47] was used for functional annotation of protein sequences, and COG functional enrichment of selected eggNOG matches was performed using the Enrichment Analysis tool of iMetaShiny[48].

Downstream data analysis

Compound structure clustering: Clustering of compounds was performed using the fingerprint, and rcdk R packages following a method developed by Voicu et al.[49] Briefly, The SMILES (Simplified Molecular Input Line Entry System) notation for each compound (excluding those without a defined chemical structure) was parsed using the parse.smiles() function from the rcdk package, then compound fingerprints were obtained by the get.fingerprint() function of the fingerprint package using type “extended” as suggested by Voicu et al.[49] Next, fp.sim.matrix() function was used to calculates the similarity matrix for the set of compound fingerprints by the Tanimoto coefficient. Finally, the compound structure similarity matrix was passed to the pvclust function, which performed hierarchical clustering and generated 100 bootstrap samples to evaluate the stability of the clustering results.

Kernel density estimation (KDE): Kernel density estimation (KDE) of the two-dimensional ARP versus nFR_p landscape was performed using the kde2d() function of R package MASS with n resolution set as 100, and 3D surface plot of the KDE results was visualized by R package plotly.

Feature set comparison: Comparison of shared features between different groups were performed using upset plot wrapped by the “Sets Explorer” in iMetaShiny[48] (https://shiny2.imetalab.ca/shiny/rstudio/SetExplorer/).

Principal component analysis: For principal component analysis of metaproteomic drug responses, protein intensity data was first log10 transformed, then normalized using the

estimateSizeFactorsForMatrix() function of the R package DeSeq2. Next, the pca() function of the pcaMethods package was used to perform PCA analysis using the nonlinear estimation by the NIPALS algorithm, allowing for the presence of missing values[29].

Finding microbial homologs of human protein drug targets: Human drug targets of our selected drugs were extracted from the comprehensive map of molecular drug targets (NIHMS80822-supplement-Supplementary_Information_S2.xlsx table in the referred paper) summarized by Santos et al.[30] *hmm* and *seed* files of each protein target were downloaded from the Pfam database[50] (https://www.ebi.ac.uk/interpro/), then hmmsearch[51] was used to perform microbial homolog sequence search by protein alignment/profile-HMM against our metaproteomic sequence database of this dataset.

Functional redundancy calculation: Within-sample taxonomic diversity (TD) and functional redundancy (FR_p) of each metaproteome was calculated using the label-free quantified dataset following our previously developed approach[25]. Briefly, the proteome-content network of each individual metaproteome data was generated according to pep2taxa-based taxonomic annotation and eggNOG-based Clusters of Orthologous Genes (COG) annotations. Genus-level biomass contributions were estimated by genus-specific peptide intensities in pep2taxa-based taxonomic annotation. Then, taxonomic diversity (TD) and functional redundancy normalized by TD (nFR_p) was calculated using the python codes provided by our previous research[25] (https://github.com/yvonnelee1988/Metaproteome_FRp).

Differential protein analysis: Differential protein expression between DMSO and the seven neurological drugs (amoxapine, duloxetine, fluoxetine, fluphenazine, fluvoxamine, paroxetine and sertraline) was analyzed using the Differential Protein Analyzer of iMetaLab Suite[48]. The functional annotation and taxonomic representatives of the resulting proteins were annotated by eggNOG mapper and visualized using Sanky plot with geom_alluvium() function of ggplot2.

PhyloFunc analysis and community state types (CST) clustering: The phylogenetic tree was constructed from a deep metagenomics dataset of individual gut microbiomes using IQ-TREE2 (http://www.iqtree.org/), the tree inference included 1000 replicates for the SH-like approximate likelihood ratio test (aLRT) and 1000 ultrafast bootstrap replicates. PhyloFunc was then computed with the phylogenetic tree and the original directLFQ-quantified protein group table, with taxonomy information annotated by referencing the metagenomic MAG and functional annotation performed by eggNOG mapper[47]. The Python package *phylofunc* [23] was then used to compute functional distances matrices across metaproteomics samples.

Other analyses and visualizations: Correlation analysis was performed using cor.test() function in the stats package. Scatter plots with aligned density plots were created by ggscatterhist()

function in the ggpubr package. Partitioning around medoids analyses were performed using pam() function in the cluster package. Taxonomic heatmap and clustering was performed using the pheatmap package.

Computation of the generalized Lotka-Volterra (gLV) model

The gLV competition model, considering between-cluster interactions can be written as follows:

$$\frac{dx_i}{dt} = f_i(\mathbf{x}) = r_i x_i \left[\frac{K_i - x_i - \left(\sum_{j\neq i}^{3} \alpha_{ij} x_j\right)}{K_i}\right] \quad (1),$$

where, i and j represent i^{th} and j^{th} microbial cluster, respectively. In our case, $1 \leq i \neq j \leq 3$. $\mathbf{x}=[x_1, x_2, x_3]$ represents the population size of each microbial cluster. The parameters r_i, K_i and α_{ij} represent the intrinsic growth rate of the ith microbial cluster, environmental carrying capacity of the ith microbial cluster, and competition coefficient from the jth to the ith microbial cluster, respectively. We note that the stable state is dependent on model parameters r_i, K_i and α_{ij} rather than the initial population size of each microbial cluster. Based on the gLV competition model considering between-cluster interactions given by equation (1), we can calculate population sizes at the equilibrium state where $\frac{dx_i}{dt} = 0$. Therefore, at equilibrium, we have:

$$x_i^* = K_i - \sum_{j\neq i}^{3} \alpha_{ij} x_j \quad (2)$$

Based on Lyapunov's indirect method, the Jacobian matrix $\mathbf{J}$ of the gLV model at the equilibrium point $\mathbf{x}^*=[x^*_1, x^*_2, x^*_3]$ can be obtained. By linearizing equation (1) around $\mathbf{x}^*$ and its neighborhood, it is then transformed into a linear dynamic model:

$$\frac{d\mathbf{x}}{dt} = \mathbf{J}\mathbf{x} \quad (3)$$

Where,

$$\mathbf{J} = J_{ij} = \frac{\partial f_i(\mathbf{x})}{\partial x_j} \quad (4)$$

If all eigenvalues of the matrix $\mathbf{J}$ lie in the left half of the complex plane, then we achieve a stable equilibrium point of the gLV model.

Ordinary equation of the gLV model was solved using scipy.integrate function odeint() in Jupyter Notebook running Python 3. And visualization of model dynamics was performed using matplotlib.pyplot.plot().

Functional redundancy enhancement to combat ARP response

An additional RapidAIM test was performed to investigate the impact of enhanced functional redundancy on mitigating drug-induced ARP within microbial communities. First, to evaluate the

impact of FOS on functional redundancy, three additional individual microbiomes were initially screened for their response of nFR_p to 1 mg/mL of FOS treatment. The microbiome exhibiting a high increase in nFR_p was selected for further analysis. It was subjected to 250 μM sertraline, 1 mg/mL FOS, or 250 μM sertraline + 1 mg/mL FOS in 25 μL DMSO, and blank (25 μL DMSO only) treatments for 48 hours of culturing, followed by metaproteomic analyses to assess changes in functional redundancy and ARP levels in different groups. Technical triplicates were performed for each group.

DATA AND CODE AVAILABILITY

- All metaproteomics data sets reported in this study have been deposited at ProteomeXchange database through the PRIDE repository and will be publicly available as of the date of publication.
- The metagenomics data used in this study are deposited in the NCBI Sequence Read Archive (SRA).
- Metaproteomics response Shiny app is available at https://shiny.imetalab.ca/MPR_Viz/.
- This paper does not report original code.
- Any additional information required to reanalyze the data reported in this paper is available from the lead contact (Daniel Figeys, dfigeys@uottawa.ca) upon request.

MATERIALS AVAILABILITY

No materials were generated in the study.

ACKNOWLEDGMENTS

D.F. acknowledges funding from Genome Canada, the Province of Ontario and NSERC. L.L acknowledges funding from National Natural Science Foundation of China (grant 32370050). We would like to thank Dr. Dawei Hu for his advice and help on the gLV model, and Dr. Yangyu Liu for his advice on functional redundancy analysis. The authors also acknowledge technical support platforms and staffs at the Faculty of Medicine, University of Ottawa and National Center for Protein Sciences (Beijing) for providing essential resources and assistance.

DECLARATION OF INTERESTS

D.F. and A.S. are co-founders of MedBiome Inc., a microbiome nutrition and therapeutic company. C.M.A.S. is currently a staff at Recursion Pharmaceuticals, and K.W. is currently a staff

at Carleton University, the presented contribution in this manuscript was made during their employment at the University of Ottawa. Other co-authors declare no conflict of interest.

AUTHOR CONTRIBUTIONS

D.F. and L.L. designed and supervised the study, and wrote the manuscript; M.H., C.M.A.S., L.L., Xu Z. and D.F. selected compounds for this study. J.M., Xu Z., K.W. and H.Q. recruited healthy volunteers, collected individual fecal samples, collected written consent and biobanked the samples. M.H. and L.L. prepared the therapeutic compound library. L.L. established, validated, and performed the RapidAIM in vitro culturing and metaproteomic sample processing workflows, during which process, J.M., K.W., M.H. and H.Q. assisted with microbiome culturing and microbial cell washing. L.L. and Xin Z. performed the functional redundancy enhancement experiment. Z.N. optimized LC-MS/MS parameters, both Z.N. and L.L. performed the metaproteomic LC-MS/MS analysis and tracked LC-MS/MS performance. L.L., K.C. and C.M.A.S. performed metaproteomic database search. J.B. and A.S. performed metagenomic sample processing and sent samples for Illumina NovaSeq analysis. J.M.S. performed metagenomic data analysis and created metagenomics-based protein databases. L.L. and C.M.A.S curated the data and performed TMT metaproteomics data analysis and compound structure clustering. L.L. performed all label-free metaproteomics down-stream data analysis. All authors contributed to the writing, editing, and proofreading of the manuscript.

REFERENCES

1. Lam, K.N., Alexander, M., and Turnbaugh, P.J. (2019). Precision Medicine Goes Microscopic: Engineering the Microbiome to Improve Drug Outcomes. Cell Host Microbe *26*, 22–34. https://doi.org/10.1016/j.chom.2019.06.011.

2. Maier, L., Pruteanu, M., Kuhn, M., Zeller, G., Telzerow, A., Anderson, E.E., Brochado, A.R., Fernandez, K.C., Dose, H., Mori, H., et al. (2018). Extensive impact of non-antibiotic drugs on human gut bacteria. Nature *555*, 623–628. https://doi.org/10.1038/nature25979.

3. Vich Vila, A., Collij, V., Sanna, S., Sinha, T., Imhann, F., Bourgonje, A.R., Mujagic, Z., Jonkers, D.M.A.E., Masclee, A.A.M., Fu, J., et al. (2020). Impact of commonly used drugs on the composition and metabolic function of the gut microbiota. Nat Commun *11*, 362. https://doi.org/10.1038/s41467-019-14177-z.

841 4. Li, L., Ning, Z., Zhang, X., Mayne, J., Cheng, K., Stintzi, A., and Figeys, D. (2020b). RapidAIM: a culture-
842 and metaproteomics-based Rapid Assay of Individual Microbiome responses to drugs. Microbiome *8*,
843 33. https://doi.org/10.1186/s40168-020-00806-z.

844 5. Javdan, B., Lopez, J.G., Chankhamjon, P., Lee, Y.-C.J., Hull, R., Wu, Q., Wang, X., Chatterjee, S., and
845 Donia, M.S. (2020). Personalized Mapping of Drug Metabolism by the Human Gut Microbiome. Cell
846 *181*, 1661-1679.e22. https://doi.org/10.1016/j.cell.2020.05.001.

847 6. Zimmermann, M., Zimmermann-Kogadeeva, M., Wegmann, R., and Goodman, A.L. (2019). Mapping
848 human microbiome drug metabolism by gut bacteria and their genes. Nature *570*, 462–467.
849 https://doi.org/10.1038/s41586-019-1291-3.

850 7. Noto Guillen, M., Li, C., Rosener, B., and Mitchell, A. (2024). Antibacterial activity of nonantibiotics is
851 orthogonal to standard antibiotics. Science *384*, 93–100. https://doi.org/10.1126/science.adk7368.

852 8. Bottery, M.J., Matthews, J., Wood, A.J., Krogh Johansen, H., Pitchford, J., and Friman, V.-P. (2022).
853 Inter-species interactions alter antibiotic efficacy in bacterial communities. ISME J *16*, 812–821.
854 https://doi.org/10.1038/s41396-021-01130-6.

855 9. Yu, J.S.L., Correia-Melo, C., Zorrilla, F., Herrera-Dominguez, L., Wu, M.Y., Hartl, J., Campbell, K., Blasche,
856 S., Kreidl, M., Egger, A.-S., et al. (2022). Microbial communities form rich extracellular metabolomes
857 that foster metabolic interactions and promote drug tolerance. Nat Microbiol *7*, 542–555.
858 https://doi.org/10.1038/s41564-022-01072-5.

859 10. Lindsay, R.J., Jepson, A., Butt, L., Holder, P.J., Smug, B.J., Gudelj, I., and Chase, J. (2021). Would that it
860 were so simple: Interactions between multiple traits undermine classical single-trait-based
861 predictions of microbial community function and evolution. Ecol Lett *24*, 2775–2795.
862 https://doi.org/10.1111/ele.13861.

863 11. Flynn, J.M., Cameron, L.C., Wiggen, T.D., Dunitz, J.M., Harcombe, W.R., and Hunter, R.C. (2020).
864 Disruption of cross-feeding inhibits pathogen growth in the sputa of patients with cystic fibrosis.
865 mSphere *5*, e00343-20. https://doi.org/10.1128/mSphere.00343-20.

866 12. Garcia-Santamarina, S., Kuhn, M., Devendran, S., Maier, L., Driessen, M., Mateus, A., Mastrorilli, E.,
867 Brochado, A.R., Savitski, M.M., Patil, K.R., et al. (2023). Emergence of community behaviors in the gut
868 microbiota upon drug treatment. Preprint at bioRxiv, https://doi.org/10.1101/2023.06.13.544832
869 https://doi.org/10.1101/2023.06.13.544832.

870 13. Bottery, M.J., Pitchford, J.W., and Friman, V.-P. (2021). Ecology and evolution of antimicrobial
871 resistance in bacterial communities. ISME J *15*, 939–948. https://doi.org/10.1038/s41396-020-00832-
872 7.

873 14. Gotfryd, K., Boesen, T., Mortensen, J.S., Khelashvili, G., Quick, M., Terry, D.S., Missel, J.W., LeVine,
874 M.V., Gourdon, P., Blanchard, S.C., et al. (2020). X-ray structure of LeuT in an inward-facing occluded
875 conformation reveals mechanism of substrate release. Nat Commun *11*, 1005.
876 https://doi.org/10.1038/s41467-020-14735-w.

877 15. Zhou, Z., Zhen, J., Karpowich, N., Law, C., Reith, M., and Wang, D. (2009). Antidepressant Specificity of
878 Serotonin Transporter Suggested by Three LeuT-SSRI Structures. Nat Struct Mol Biol *16*.
879 https://doi.org/10.1038/nsmb.1602.

880 16. Fujita, H., Ushio, M., Suzuki, K., Abe, M.S., Yamamichi, M., Iwayama, K., Canarini, A., Hayashi, I.,
881 Fukushima, K., Fukuda, S., et al. (2023). Alternative stable states, nonlinear behavior, and
882 predictability of microbiome dynamics. Microbiome *11*, 63. https://doi.org/10.1186/s40168-023-
883 01474-5.

884 17. Beisner, B., Haydon, D., and Cuddington, K. (2003). Alternative stable states in ecology. Front Ecol
885 Environ *1*, 376–382. https://doi.org/10.1890/1540-9295(2003)001[0376:ASSIE]2.0.CO;2.

886 18. Louca, S., Polz, M.F., Mazel, F., Albright, M.B.N., Huber, J.A., O'Connor, M.I., Ackermann, M., Hahn,
887 A.S., Srivastava, D.S., Crowe, S.A., et al. (2018). Function and functional redundancy in microbial
888 systems. Nat Ecol Evol *2*, 936–943. https://doi.org/10.1038/s41559-018-0519-1.

889 19. Biggs, C.R., Yeager, L.A., Bolser, D.G., Bonsell, C., Dichiera, A.M., Hou, Z., Keyser, S.R., Khursigara, A.J.,
890 Lu, K., Muth, A.F., et al. (2020). Does functional redundancy affect ecological stability and resilience?
891 A review and meta-analysis. Ecosphere *11*, e03184. https://doi.org/10.1002/ecs2.3184.

892 20. Zhang, X., Walker, K., Mayne, J., Li, L., Ning, Z., Stintzi, A., and Figeys, D. (2022). Evaluating live
893 microbiota biobanking using an *ex vivo* microbiome assay and metaproteomics. Gut Microbes *14*,
894 2035658. https://doi.org/10.1080/19490976.2022.2035658.

895 21. Creskey, M., Li, L., Ning, Z., Brown, E.E., Mayne, J., Walker, K., Ampaw, A., Ben, R., Zhang, X., and
896 Figeys, D. (2022). An economic and robust TMT labeling approach for high throughput proteomic and
897 metaproteomic analysis. Proteomics *Online ahead of print*, e2200116.

898 22. Li, L., Mayne, J., Beltran, A., Zhang, X., Ning, Z., and Figeys, D. (2024). RapidAIM 2.0: a high-throughput
899 assay to study functional response of human gut microbiome to xenobiotics. Microbiome Res Rep *3*,
900 26. https://doi.org/10.20517/mrr.2023.57.

901 23. Wang, L., Simopoulos, C.M.A., Serrana, J.M., Ning, Z., Sun, B., Yuan, J., Figeys, D., and Li, L. (2024).
902 PhyloFunc: Phylogeny-informed Functional Distance as a New Ecological Metric for Metaproteomic
903 Data Analysis. Preprint at bioRxiv, https://doi.org/10.1101/2024.05.28.596184
904 https://doi.org/10.1101/2024.05.28.596184.

905 24. Fuentes, A., Pineda, M., and Venkata, K. (2018). Comprehension of Top 200 Prescribed Drugs in the
906 US as a Resource for Pharmacy Teaching, Training and Practice. Pharmacy *6*, 43.
907 https://doi.org/10.3390/pharmacy6020043.

908 25. Li, L., Wang, T., Ning, Z., Zhang, X., Butcher, J., Serrana, J.M., Simopoulos, C.M.A., Mayne, J., Stintzi, A.,
909 Mack, D.R., et al. (2023). Revealing proteome-level functional redundancy in the human gut
910 microbiome using ultra-deep metaproteomics. Nat Commun *14*, 3428.
911 https://doi.org/10.1038/s41467-023-39149-2.

912 26. Zhang, X., Ning, Z., Mayne, J., Moore, J.I., Li, J., Butcher, J., Deeke, S.A., Chen, R., Chiang, C.-K., Wen,
913 M., et al. (2016). MetaPro-IQ: a universal metaproteomic approach to studying human and mouse gut
914 microbiota. Microbiome *4*, 31. https://doi.org/10.1186/s40168-016-0176-z.

915 27. Ammar, C., Schessner, J.P., Willems, S., Michaelis, A.C., and Mann, M. (2023). Accurate Label-Free
916 Quantification by directLFQ to Compare Unlimited Numbers of Proteomes. Mol Cell Proteomics *22*,
917 100581. https://doi.org/10.1016/j.mcpro.2023.100581.

918 28. Voß, H., Schlumbohm, S., Barwikowski, P., Wurlitzer, M., Dottermusch, M., Neumann, P., Schlüter, H.,
919 Neumann, J.E., and Krisp, C. (2022). HarmonizR enables data harmonization across independent
920 proteomic datasets with appropriate handling of missing values. Nat Commun *13*, 3523.
921 https://doi.org/10.1038/s41467-022-31007-x.

922 29. Wold, H. (1966). Estimation of principal components and related models by iterative least squares. In
923 Multivariate Analysis, P. R. Krishnajah, ed. (Academic Press), pp. 391–420.

924 30. Santos, R., Ursu, O., Gaulton, A., Bento, A.P., Donadi, R.S., Bologa, C.G., Karlsson, A., Al-Lazikani, B.,
925 Hersey, A., Oprea, T.I., et al. (2017). A comprehensive map of molecular drug targets. Nat Rev Drug
926 Discov *16*, 19–34. https://doi.org/10.1038/nrd.2016.230.

927 31. Gonze, D., Lahti, L., Raes, J., and Faust, K. (2017). Multi-stability and the origin of microbial
928 community types. ISME J *11*, 2159–2166. https://doi.org/10.1038/ismej.2017.60.

929 32. Zhou, Y., Zhang, Y., Zhao, D., Yu, X., Shen, X., Zhou, Y., Wang, S., Qiu, Y., Chen, Y., and Zhu, F. (2024).
930 TTD: Therapeutic Target Database describing target druggability information. Nucleic Acids Res *52*,
931 D1465–D1477. https://doi.org/10.1093/nar/gkad751.

932 33. Keilhauer, E.C., Hein, M.Y., and Mann, M. (2015). Accurate Protein Complex Retrieval by Affinity
933 Enrichment Mass Spectrometry (AE-MS) Rather than Affinity Purification Mass Spectrometry (AP-MS).
934 Mol Cell Proteomics *14*, 120–135. https://doi.org/10.1074/mcp.M114.041012.

935 34. Alcock, B.P., Huynh, W., Chalil, R., Smith, K.W., Raphenya, A.R., Wlodarski, M.A., Edalatmand, A.,
936 Petkau, A., Syed, S.A., Tsang, K.K., et al. (2023). CARD 2023: expanded curation, support for machine
937 learning, and resistome prediction at the Comprehensive Antibiotic Resistance Database. Nucleic
938 Acids Research *51*, D690–D699. https://doi.org/10.1093/nar/gkac920.

939 35. Grießhammer, A., de la Cuesta-Zuluaga, J., Zahir, T., Müller, P., Gekeler, C., Chang, H., Schmitt, K.,
940 Planker, C., Bohn, E., Nguyen, T.H., et al. (2023). Non-antibiotic drugs break colonization resistance
941 against pathogenic Gammaproteobacteria. bioRxiv, 2023.11.06.564936.
942 https://doi.org/10.1101/2023.11.06.564936.

943 36. Li, L., Abou-Samra, E., Ning, Z., Zhang, X., Mayne, J., Wang, J., Cheng, K., Walker, K., Stintzi, A., and
944 Figeys, D. (2019). An in vitro model maintaining taxon-specific functional activities of the gut
945 microbiome. Nat Commun *10*, 4146. https://doi.org/10.1038/s41467-019-12087-8.

946 37. Yan, A., Butcher, J., Schramm, L., Mack, D.R., and Stintzi, A. (2023). Multiomic spatial analysis reveals
947 a distinct mucosa-associated virome. Gut Microbes *15*, 2177488.
948 https://doi.org/10.1080/19490976.2023.2177488.

949 38. Chen, S., Zhou, Y., Chen, Y., and Gu, J. (2018). fastp: an ultra-fast all-in-one FASTQ preprocessor.
950 Bioinformatics *34*, i884–i890. https://doi.org/10.1093/bioinformatics/bty560.

951 39. Wood, D.E., Lu, J., and Langmead, B. (2019). Improved metagenomic analysis with Kraken 2. Genome
952 Biol *20*, 257. https://doi.org/10.1186/s13059-019-1891-0.

953 40. Bushnell, B. (2014). BBMap: A Fast, Accurate, Splice-Aware Aligner. In Report Number: LBNL-7065E.

954 41. Li, D., Liu, C.-M., Luo, R., Sadakane, K., and Lam, T.-W. (2015). MEGAHIT: an ultra-fast single-node
955 solution for large and complex metagenomics assembly via succinct de Bruijn graph. Bioinformatics
956 *31*, 1674–1676. https://doi.org/10.1093/bioinformatics/btv033.

957 42. Hyatt, D., Chen, G.-L., LoCascio, P.F., Land, M.L., Larimer, F.W., and Hauser, L.J. (2010). Prodigal:
958 prokaryotic gene recognition and translation initiation site identification. BMC Bioinformatics *11*, 119.
959 https://doi.org/10.1186/1471-2105-11-119.

960 43. Cheng, K., Ning, Z., Zhang, X., Li, L., Liao, B., Mayne, J., and Figeys, D. (2020). MetaLab 2.0 Enables
961 Accurate Post-Translational Modifications Profiling in Metaproteomics. J Am Soc Mass Spectrom *31*,
962 1473–1482. https://doi.org/10.1021/jasms.0c00083.

963 44. Li, J., Jia, H., Cai, X., Zhong, H., Feng, Q., Sunagawa, S., Arumugam, M., Kultima, J.R., Prifti, E., Nielsen,
964 T., et al. (2014). An integrated catalog of reference genes in the human gut microbiome. Nature
965 Biotechnology *32*, 834–841. https://doi.org/10.1038/nbt.2942.

966 45. Huang, T., Choi, M., Tzouros, M., Golling, S., Pandya, N.J., Banfai, B., Dunkley, T., and Vitek, O. (2020).
967 MSstatsTMT: Statistical Detection of Differentially Abundant Proteins in Experiments with Isobaric
968 Labeling and Multiple Mixtures. Mol Cell Proteomics *19*, 1706–1723.
969 https://doi.org/10.1074/mcp.RA120.002105.

970 46. Jagtap, P.D., Blakely, A., Murray, K., Stewart, S., Kooren, J., Johnson, J.E., Rhodus, N.L., Rudney, J., and
971 Griffin, T.J. (2015). Metaproteomic analysis using the Galaxy framework. PROTEOMICS *15*, 3553–
972 3565. https://doi.org/10.1002/pmic.201500074.

973 47. Cantalapiedra, C.P., Hernández-Plaza, A., Letunic, I., Bork, P., and Huerta-Cepas, J. (2021). eggNOG-
974 mapper v2: Functional Annotation, Orthology Assignments, and Domain Prediction at the
975 Metagenomic Scale. Molecular Biology and Evolution *38*, 5825–5829.
976 https://doi.org/10.1093/molbev/msab293.

977 48. Li, L., Ning, Z., Cheng, K., Zhang, X., Simopoulos, C.M.A., and Figeys, D. (2022). iMetaLab Suite: A one-
978 stop toolset for metaproteomics. iMeta *1*, e25. https://doi.org/10.1002/imt2.25.

979 49. Voicu, A., Duteanu, N., Voicu, M., Vlad, D., and Dumitrascu, V. (2020). The rcdk and cluster R packages
980 applied to drug candidate selection. J Cheminform *12*, 3. https://doi.org/10.1186/s13321-019-0405-0.

50. Paysan-Lafosse, T., Blum, M., Chuguransky, S., Grego, T., Pinto, B.L., Salazar, G.A., Bileschi, M.L., Bork, P., Bridge, A., Colwell, L., et al. (2023). InterPro in 2022. Nucleic Acids Res *51*, D418–D427. https://doi.org/10.1093/nar/gkac993.

51. Potter, S.C., Luciani, A., Eddy, S.R., Park, Y., Lopez, R., and Finn, R.D. (2018). HMMER web server: 2018 update. Nucleic Acids Res *46*, W200–W204. https://doi.org/10.1093/nar/gky448.

52. Xie, Z., Bailey, A., Kuleshov, M.V., Clarke, D.J.B., Evangelista, J.E., Jenkins, S.L., Lachmann, A., Wojciechowicz, M.L., Kropiwnicki, E., Jagodnik, K.M., et al. (2021). Gene Set Knowledge Discovery with Enrichr. Current Protocols *1*, e90. https://doi.org/10.1002/cpz1.90.

Supplementary Figures

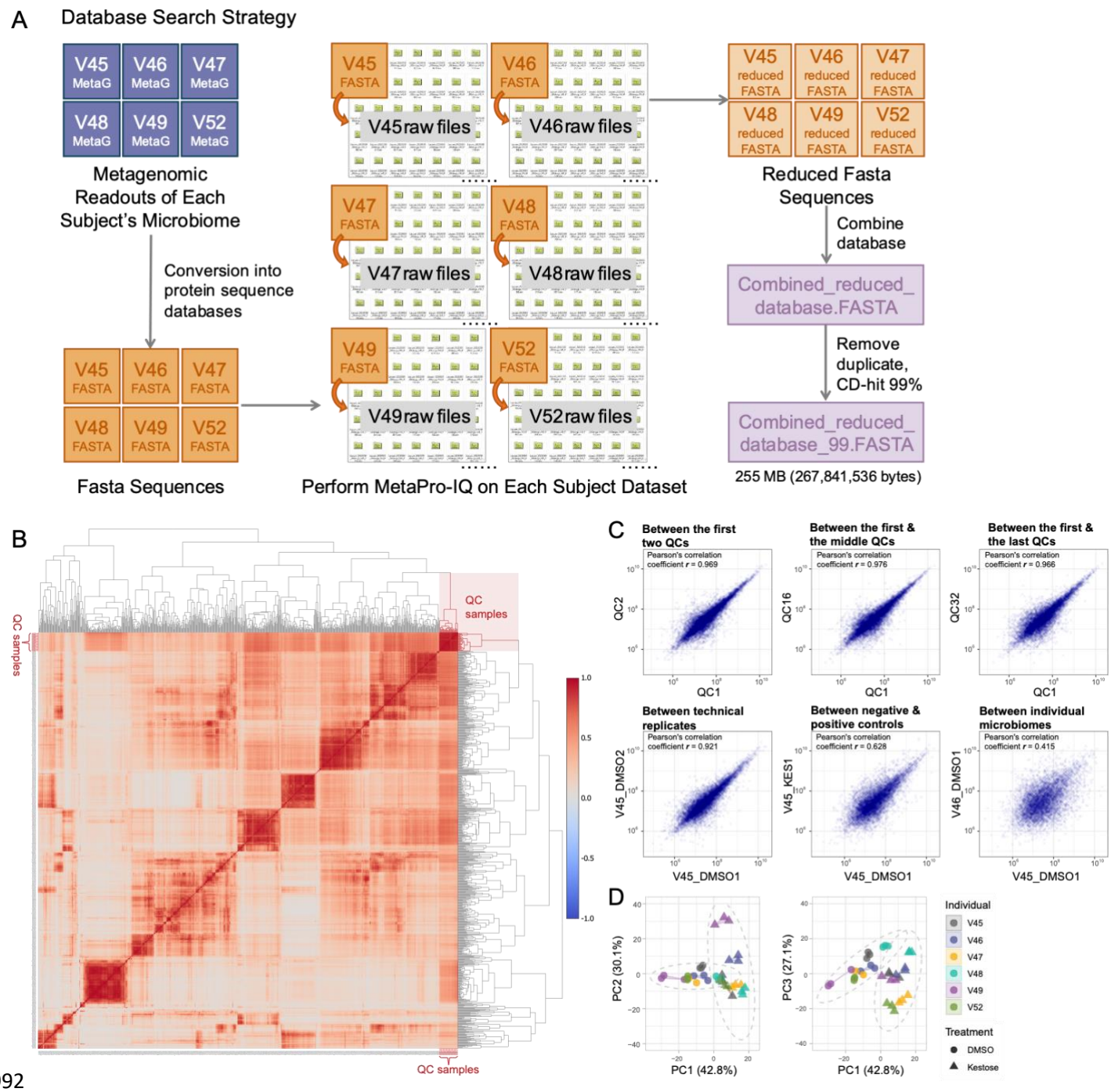

Figure S1. Database search strategy for the Label-free LC-MS/MS dataset and the dataset quality

A. Deep metagenomic data of each subject's original microbiome was converted into protein FASTA sequences using Prodigal. All LFQ raw files corresponding to each subject's cultured microbiome were subjected to the MetaPro-IQ workflow based on each corresponding database to generate individual subset-specific reduced databases. The reduced databases were combined and duplicated proteins were removed using 99% sequence identity threshold with CD-HIT. **B**. Label-free LC-MS/MS sample correlations. Heatmap and hierarchical clustering showing between-sample Pearson's correlation coefficients throughout the label-free LC-MS/MS sample analysis. Quality control (QC) samples were created by mixing an equal amount of negative control (DMSO) samples of the six individuals' microbiomes, one QC sample was inserted each day during the analysis, resulting in 32 QC samples throughout the run. All QC samples are highlighted in red on this figure. **C.** Scatter plots showing reproducibility of the study as well as divergence of different groups of samples. Scatter plot and Pearson's correlation of LFQ protein intensities between the first two QC samples; between the first QC sample and the middle QC sample; between the first QC sample and the last QC sample; between one pair of technical replicates (two cultured negative control samples of V45 is shown); between the negative and positive controls (a negative control sample vs a kestose-treated microbiome, i.e. the positive control sample of V45); between the DMSO samples of V45 and V46. **D.** PCA showing that the positive control was effective.

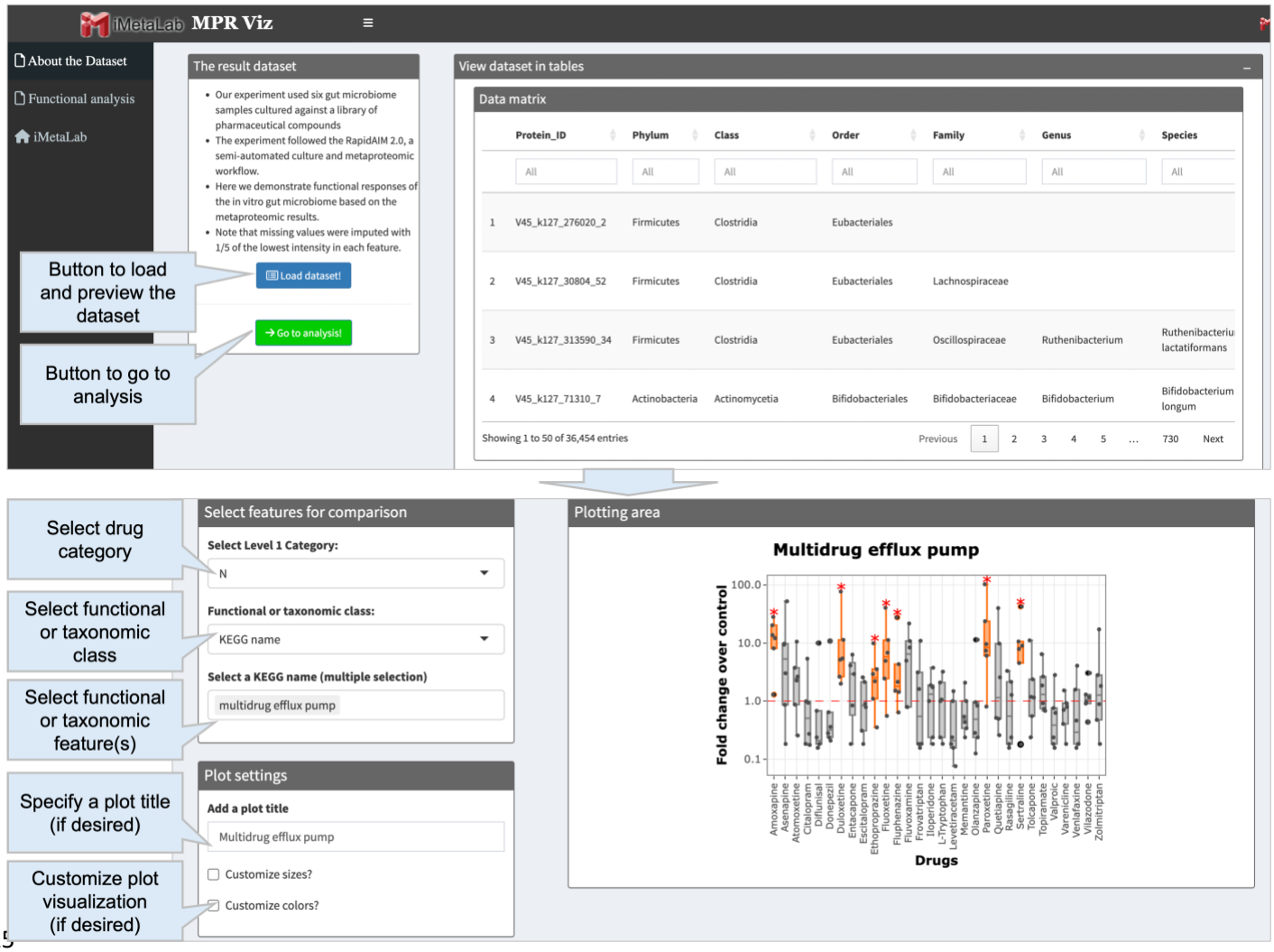

Figure S2. Interface of the Shiny app showing an example metaproteomic response visualization. The Shiny app is available at (https://shiny.imetalab.ca/MPR_Viz/). The analysis interface includes selection of drug category (at ATC level-1), functional or taxonomic annotation classes, and detailed functional or taxonomic annotation features. The plotting area is showing an example analysis on the response of microbial proteins annotated with multidrug efflux pump function to a series of N class compounds.

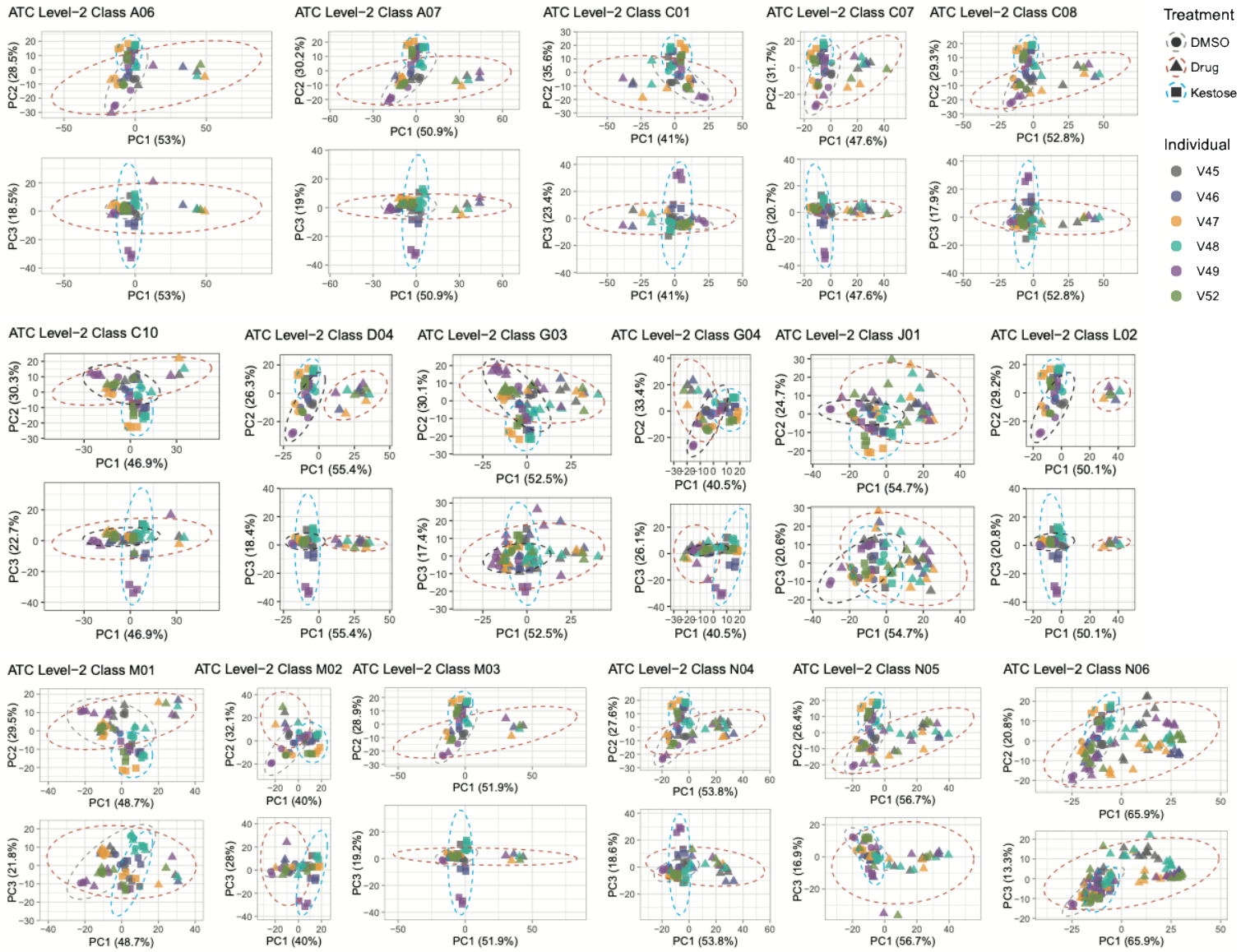

Figure S2. Metaproteomic responses to ATC level-2 subclasses that contain MPR+ compounds. Detailed drug names are listed in Supplementary Table S2.

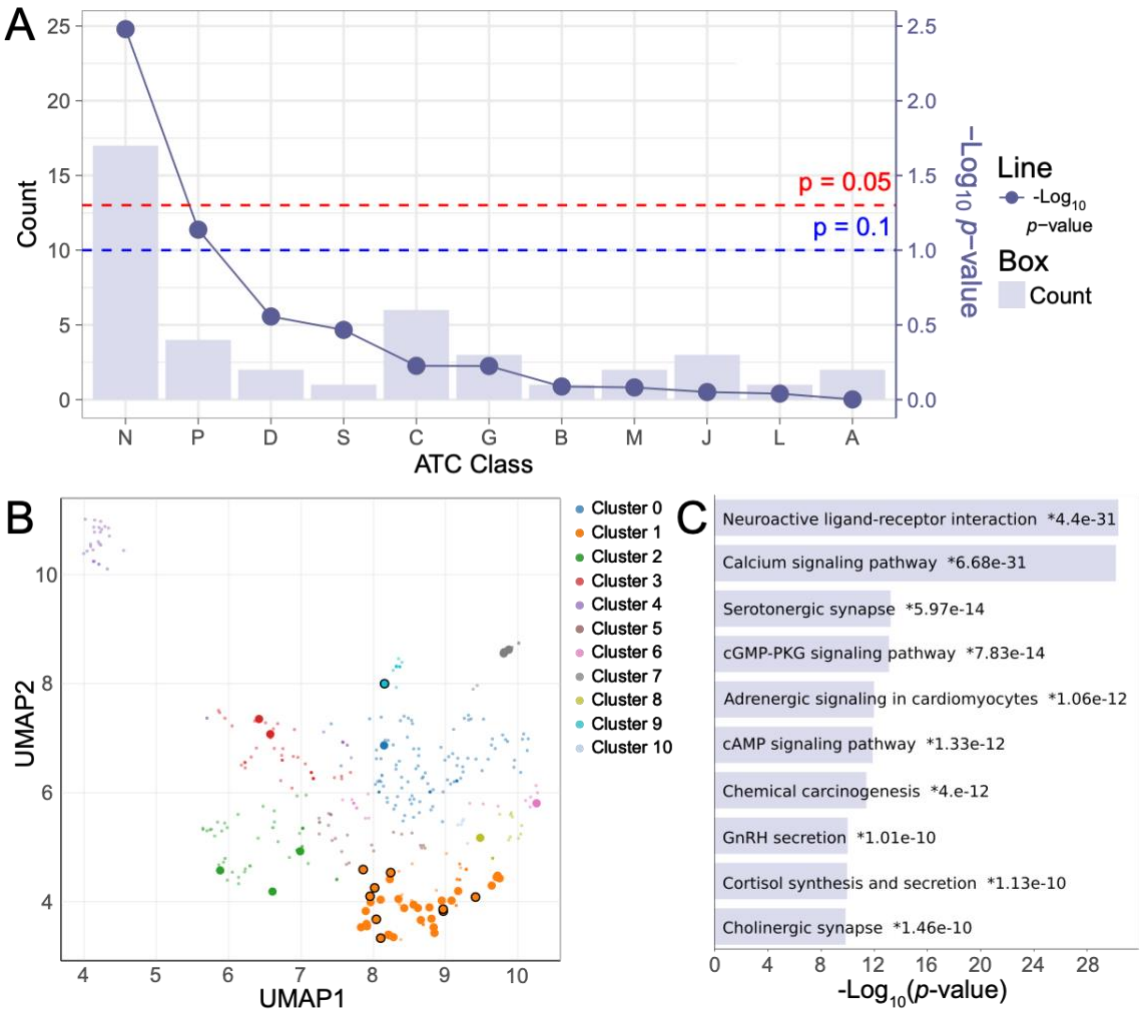

Figure S3. Enrichment analyses of MPR+ compounds. (A) Enrichment analysis of ATC level 1 class in MPR+ compounds against all 312 selected compounds. **(B)** 50 human protein targets corresponding to all MPR+ compounds were subjected to enrichment analysis against the KEGG_2021_Human gene set library. Darker and larger points, indicate more significantly enriched terms compared to genes in the library. Here we show that significantly enriched KEGG terms are concentrated in Cluster 1. **(C)** Bar plot of 10 most highly enriched terms among the 50 human protein targets against the KEGG_2021_Human gene set database. Enrichment analyses were performed using Enrichr on the Appyter platform[52].

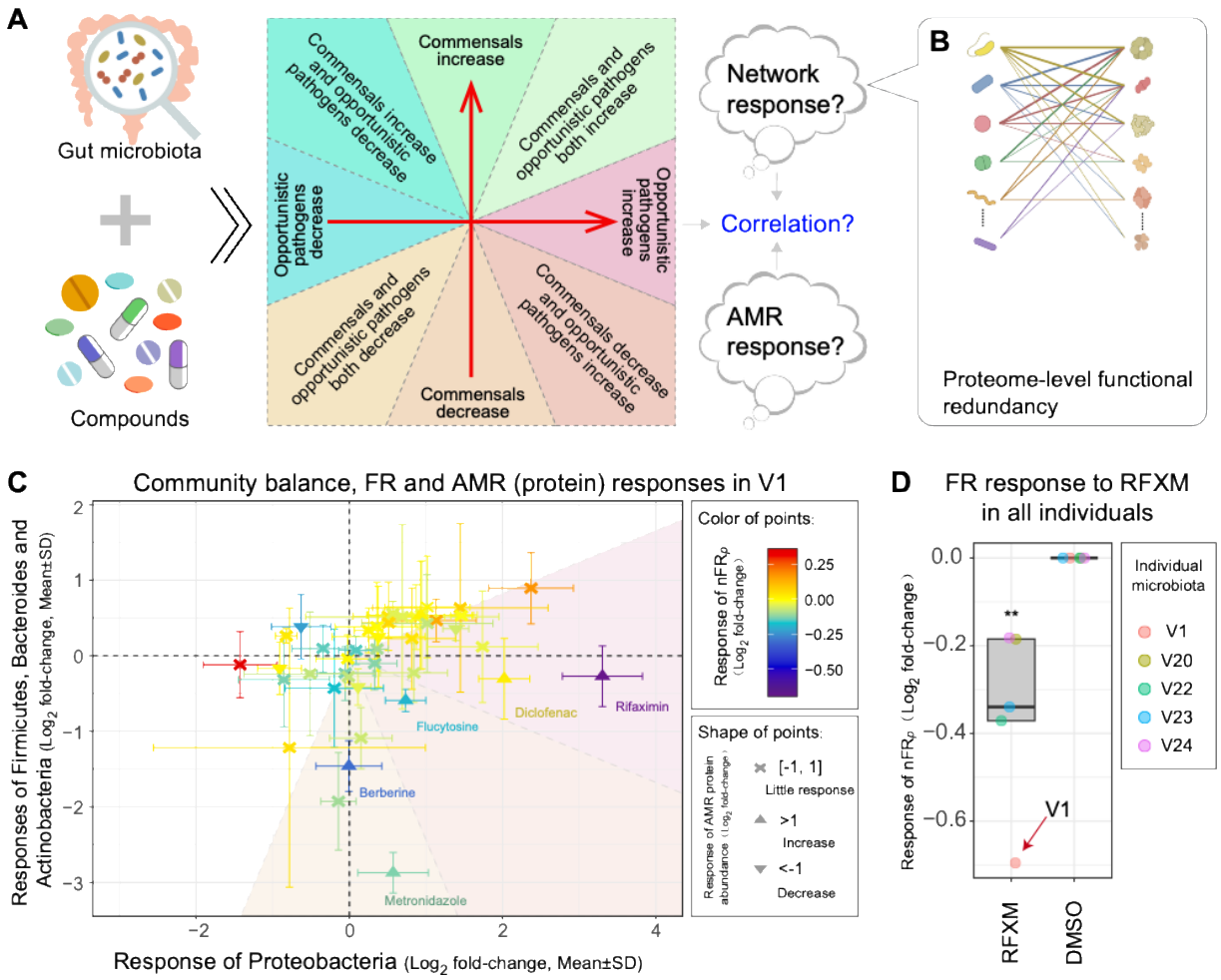

Figure S5 Re-analysis of a previously published dataset suggesting possible connection between ARP and FRp.

(A) Drug interventions on the gut microbiota can lead to changes in the balance between symbiotic bacteria and opportunistic pathogens. Therefore, we can map these changes onto a Cartesian coordinate system, dividing them into different regions (as indicated by color blocks and text annotations), to visually observe the drug response on microbiota balance. It is of interest whether samples falling into different regions correlate with the ecological properties of the community and the response of antibiotic resistance proteins. **(B)** The protein-level functional redundancy of individual microbiota samples can be quantified as described in our previous work[25]. **(C)** The normalized functional redundancy (nFR_p) and the response of antibiotic resistance proteins to multiple drugs in the gut microbiota of individual V1 from our previous dataset[4] was calculated and presented on the community balance map. We visualized the protein

biomass along the x-axis representing the response of the Proteobacteria phylum (now referred to as Pseudomonadota in the updated NCBI taxonomy), which is rich in opportunistic pathogens, and the y-axis representing the response of the Firmicutes (Bacillota), Bacteroidetes (Bacteroidota), and Actinobacteria (Actinomycetota) phyla, which are primarily symbiotic bacteria. A Log_2 fold-change >1 indicates that the abundance of antibiotic resistance proteins after drug treatment is more than twice that of the DMSO control group. (D) In all five individuals in the previous dataset[4], the functional redundancy of their gut microbiota showed significant reductions under rifaximin (RFXM) treatment, with individual V1 exhibiting the largest reduction (indicated by the red arrow).

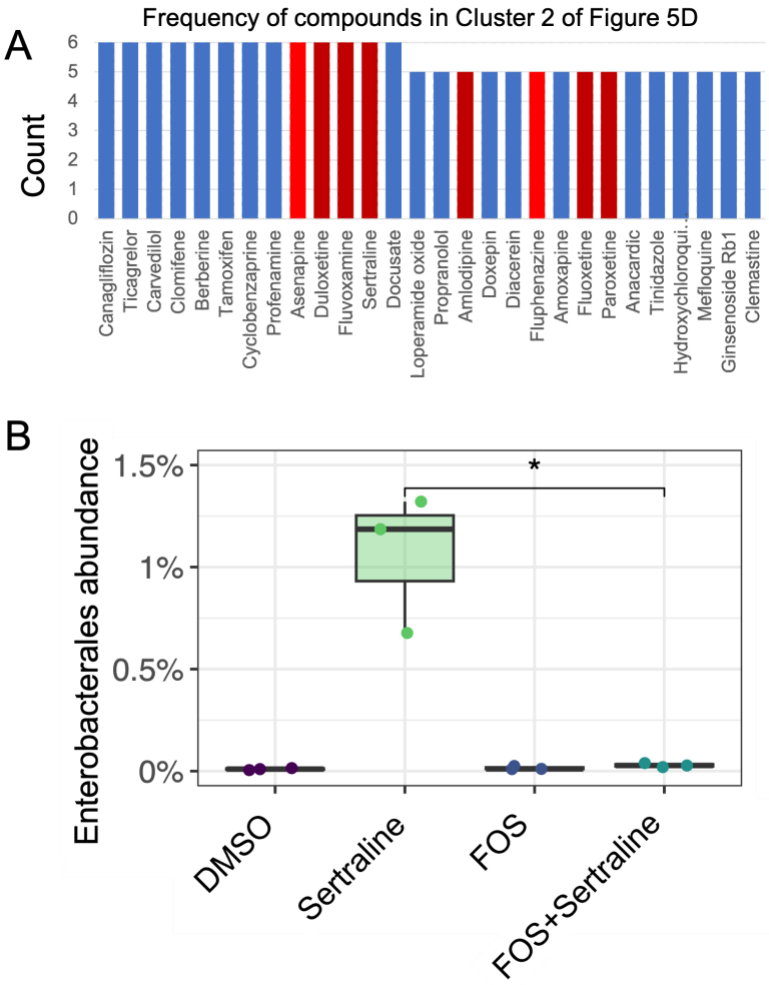

Figure S6 Sertraline increased ARP, reduced FRp, and elevated Enterobacteriales abundance. (A) Frequency of drugs in cluster 2 of the six ARP vs FRp plots (as in Figure 5D) showing Sertraline increased ARP and reduced FRp in all six individual microbiomes. **(B)** Sertraline increased Enterobacterales abundance, and this increase was reversed by the addition of FOS.